Check for updates

Geochemistry, Geophysics, Geosystems®

AGU ADVANCING EARTH AND SPACE SCIENCES

REVIEW ARTICLE
10.1029/2024GC011567

Special Collection:
Frontiers in lithospheric dynamics: bridging scales through observations, experiments, and computations

Open Access GNSS Data for Studies of the Lithosphere

D. Sarah Stamps[1] and **Corné Kreemer**[2]

[1]Department of Geosciences, Virginia Tech, Blacksburg, VA, USA, [2]Nevada Bureau of Mines and Geology and Nevada Seismological Laboratory, University of Nevada, Reno, Reno, NV, USA

Key Points:

- Describe various types of Global Navigation Satellite System (GNSS) data and their uses for studying the lithosphere
- Review of the treatment of GNSS data required for lithospheric studies
- Provide information about numerous open access GNSS data resources

Correspondence to:
D. S. Stamps,
dstamps@vt.edu

Citation:
Stamps, D. S., & Kreemer, C. (2024). Open access GNSS data for studies of the lithosphere. *Geochemistry, Geophysics, Geosystems*, *25*, e2024GC011567. https://doi.org/10.1029/2024GC011567

Received 12 MAR 2024
Accepted 21 JUN 2024

Author Contributions:
Conceptualization: D. Sarah Stamps, Corné Kreemer
Project administration: D. Sarah Stamps, Corné Kreemer
Resources: D. Sarah Stamps, Corné Kreemer
Visualization: D. Sarah Stamps, Corné Kreemer
Writing – original draft: D. Sarah Stamps, Corné Kreemer
Writing – review & editing: D. Sarah Stamps, Corné Kreemer

© 2024 The Author(s). Geochemistry, Geophysics, Geosystems published by Wiley Periodicals LLC on behalf of American Geophysical Union.
This is an open access article under the terms of the Creative Commons Attribution License, which permits use, distribution and reproduction in any medium, provided the original work is properly cited.

Abstract Various types of Global Navigation Satellite System (GNSS) data are used for a wide range of applications. When modeled correctly, millimeter precision daily GNSS position time-series yield velocities and other derived products that can be used for investigations of lithospheric processes and properties. In this review paper, we describe the specific types of GNSS data and data products that are valuable for studies of the lithosphere, such as coseismic offsets, post-seismic decay in time-series, seasonal signals, secular velocities, and strain rates, and how those data are derived. We also discuss the applications of several types of GNSS data and data products. We provide open access resources for precision GNSS daily position time-series, quality secular velocity solutions, and daily GNSS RINEX files for researchers interested in processing their own data.

Plain Language Summary Measurements of how the surface of the Earth moves can be made with millimeter precision using Global Navigation Satellite System (GNSS) data. Several different types of GNSS-derived data can be used to study the relatively rigid outer layers of the Earth known as the lithosphere. In this review paper, we detail how GNSS data that are relevant for lithospheric studies are determined, including what corrections and errors must be considered. We describe several applications of certain GNSS data, such as quantifying tectonic plate motions. At the end of the paper, we provide numerous open access resources for GNSS data and data products that are valuable for studies of the Earth's lithosphere.

1. Introduction

Various properties of the Earth's lithosphere, which comprises crust and mantle lithospheres, as well as a wide range of dynamic processes that deform it, can be studied using high precision geodetic data from in situ Global Navigation Satellite Systems (GNSS) observations of surface motions (Figure 1). From a top-down perspective, processes such as earthquake cycle deformation (e.g., Chlieh et al., 2004; Hammond, Blewitt, Kreemer, Koehler, & Dee, 2021; Lisowski et al., 1990; K. Wang et al., 2012), plate boundary deformation (e.g., Árnadóttir et al., 2006; Koulali et al., 2011; Kreemer et al., 2014; Stamps et al., 2018), and tectonic plate motions (e.g., Altamimi et al., 2023; DeMets et al., 2000; Kogan & Steblov, 2008; Saria et al., 2013) can be constrained with GNSS observations. From a bottom up perspective, lithospheric deformation associated with deeper processes can also be investigated with geodetic data like the rheology of the (sub)lithospheric mantle (e.g., Argus et al., 2021; Hu et al., 2016; Park et al., 2023), glacial isostatic adjustment (GIA, e.g., Argus, Fu, & Landerer, 2014; Argus, Peltier, et al., 2014; J. L. Elliott et al., 2010; Hu & Freymueller, 2019; Sella et al., 2007), dynamic topography (e.g., Faccenna et al., 2014), and uplift from a mantle plume (Kreemer et al., 2020). Specific scientific questions associated with the lithosphere addressed with GNSS observations, often combined with numerical modeling, include: How is strain accommodated during the earthquake cycle? What is the geometry and angular rotation rate of tectonic plates and microplates (or crustal blocks)? How does sublithospheric mantle flow, such as uplift from plumes or coupling to horizontal tractions, influence deformation at the Earth's surface? How is strain partitioned at plate boundaries? What is the influence of GIA on surface deformation? Do large earthquakes influence tectonic plate motions? What is the rheology of the crust and upper mantle (i.e., mantle lithosphere and asthenosphere)?

In this review paper, we describe how GNSS observations useful for lithospheric investigations are derived and the various ways GNSS observations are being used to inform scientific studies pertaining to the structure, kinematics, and dynamics of the lithosphere. We introduce the different types of GNSS-derived data used for lithospheric investigations (time-series, coseismic offsets and displacements, postseismic signals and cumulative displacements, secular velocities, strain rates, seasonal signals), discuss the corrections applied to time-series data, and present what insights can be gained from high-precision position time-series, velocities, and other derived products. We also describe how GNSS observations are being used to constrain crustal motions,

15252027, 2024, 7, Downloaded from https://agupubs.onlinelibrary.wiley.com/doi/10.1029/2024GC011567, Wiley Online Library on [16/07/2024]. See the Terms and Conditions (https://onlinelibrary.wiley.com/terms-and-conditions) on Wiley Online Library for rules of use; OA articles are governed by the applicable Creative Commons License

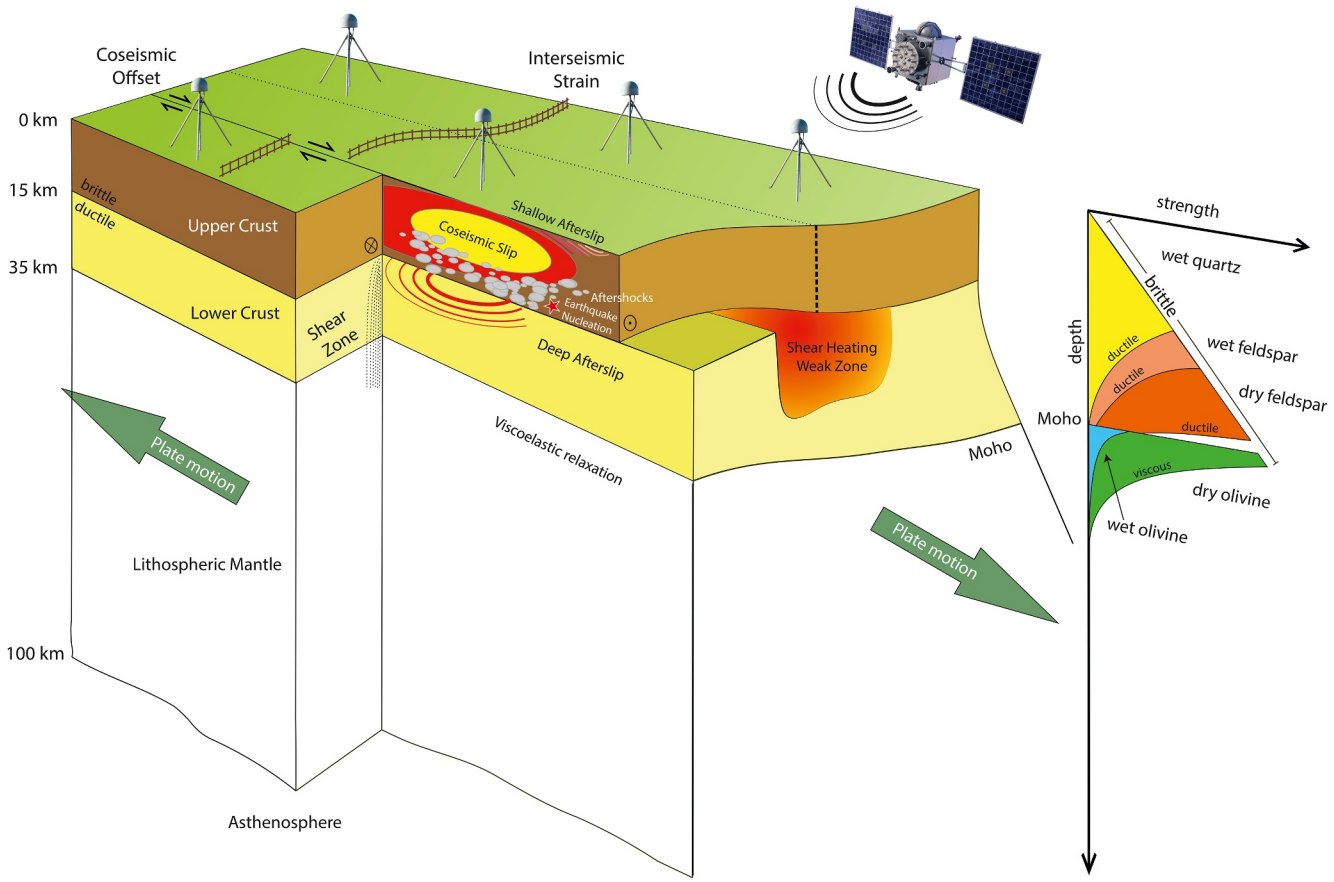

Figure 1. Modified from England et al. (2016, Figure 8). Left: Conceptual model of a strike-slip fault setting depicting a two-layered crust and lithospheric mantle with the asthenosphere below. A Global Navigation Satellite System (GNSS) satellite transmits signals to GNSS stations that are positioned at the surface to capture the earthquake cycle and provide constraints on subsurface rheological properties and processes. Right: Generic strength profile of a two-layer crust and the upper mantle. The various colors represent strengths given different material properties (i.e., wet and dry feldspar in a ductile lower crust).

lithospheric deformation, and viscoelastic relaxation. Finally, this paper provides a resources section where open access GNSS data and data products can be found.

2. Precise Position Estimates

Although three types of measurements can be derived from GNSS signals (pseudorange, doppler, and carrier phase), we focus on the carrier phase measurement to estimate the position since it is the only one capable of producing millimeter precision positions when using post-processing techniques. The GNSS carrier phase observation equation, sometimes called the GNSS equation, is (Teunissen & Montenbruck, 2017):

$$\varphi_r^s = \rho_r^s + c(dt_r - dt^s) + T_r^s + I_r^s + \lambda M_r^s + \epsilon_r^s \quad (1)$$

where index s is the satellite, index r is the receiver, φ_r^s represents the carrier phase observation, ρ_r^s is the pseudorange, c is the speed of light, dt_r and dt^s are the receiver and satellite clock offsets, T_r^s is the tropospheric delay, I_r^s represents the delay from ionospheric propagation, λ is the wavelength of the carrier, $M_r^s = N_r^s + \delta_r - \delta^s$ which sums the integer carrier-phase ambiguity in cycles (N_r^s) and the phase delays of the instrumental receiver (δ_r) and satellite (δ^s), and ϵ_r^s represents additional errors such as multipath, receiver noise, and other effects. To solve Equation 1 for millimeter precision positions, which are contained in the pseudorange (ρ_r^s), knowledge of the precise satellite positions and satellite clock parameters, commonly known as final orbits, is required. A typical workflow for calculating satellite orbits includes analyzing tracking data obtained by a network of global GNSS receivers and detailed modeling of numerous processes and parameters that affect satellite orbit

15252027, 2024, 7, Downloaded from https://agupubs.onlinelibrary.wiley.com/doi/10.1029/2024GC011567, Wiley Online Library on [16/07/2024]. See the Terms and Conditions (https://onlinelibrary.wiley.com/terms-and-conditions) on Wiley Online Library for rules of use; OA articles are governed by the applicable Creative Commons License

calculations such as Earth's orientation, relativistic effects, and spacecraft properties (Weiss et al., 2017). Several processing groups globally produce final orbits (e.g., the International GNSS Service, GFZ Potsdam, Massachusetts Institute of Technology, Jet Propulsion Laboratory (JPL), and the Scripps Orbit and Permanent Center), which are typically released after one to 2 weeks of processing. Obtaining millimeter precision positions on Earth also requires estimating or modeling each component of the right hand side of Equation 1. For example, phase ambiguities (M_r^s) are determined by levering pseudoranges, and additional effects (ϵ_r^s) such as ocean tidal loading (OTL), Earth orientation parameters, and Earth tides are precisely modeled.

Two types of post-processing approaches are used to obtain the millimeter precision positions needed for lithospheric deformation studies (Bock & Melgar, 2016; He et al., 2017): (a) Precise Point Positioning (PPP; Zumberge et al., 1997) and (b) differential carrier phase positioning, also known as network positioning (Blewitt, 1989; D. N. Dong & Bock, 1989). Teunissen and Montenbruck (2017) conceptualize PPP positioning using single GNSS station data to perform a back substitution into an International Terrestrial Reference Frame (ITRF) solution that is constrained by final orbits and the conventions used to produce final orbits. The PPP post-processing method provides estimates of absolute positions in an ITRF, and the technique does not require nearby GNSS control monuments. As noted above, well constrained satellite positions and satellite clock parameters are required. Additionally, the PPP method must adhere to the standards used for producing final orbits, such as the conventions of the International Earth Rotation and Reference System Service (IERS). Differential carrier phase positioning, or network positioning, dates back to the 1980s and uses one or more nearby control stations to perform its double—differencing mathematical approach to calculate baselines between stations simultaneously observing the same satellites. Double—differencing involves first forming a single—difference between two or more receivers that observe the same satellite. A double—difference is then formed by differencing the single differences between pairs of satellites. This classic approach produces positions in an ITRF, typically with slightly higher precision than the PPP method but with much higher computational costs. For more details about the PPP and differential carrier phase positioning post-processing methods, we refer readers to Bock and Melgar (2016), Teunissen and Montenbruck (2017), and references therein.

It is important to note that the precision of GNSS positions can be highly variable depending on whether they were obtained from either continuous GNSS stations (cGNSS) or episodic (also known as campaign) GNSS observations (eGNSS). cGNSS are permanent or semi-permanent stations that collect data nearly continuously, typically every 15 or 30 s for 24 hr considering Coordinated Universal Time (UTC) time. cGNSS can have several types of monumentation styles (Figures 2a–2c) with highly variable stability metrics (e.g., Combrinck & Schmidt, 1998; Haas et al., 2013; King & Williams, 2009; King et al., 2012). Data collection for eGNSS is for shorter, repeated time periods, such as days to weeks for one epoch. Then, there is a repeated observation some period of time later, such as 1 and 2 years between each epoch. eGNSS observations typically last 24–72 hr aligned with UTC periods. Similar to the cGNSS, the style of monumentation can vary widely (Figures 2d–2f). Positions produced from eGNSS observations typically have lower precision compared to positions derived from cGNSS.

3. Time-Series Analysis and Parameter Estimation

GNSS position time-series are normally given as daily estimates, but for some applications (particularly related to earthquake research) higher rate sampling, such as 5-min or 1 Hz, are considered as well. The station motion model $y(t)$ that is typically fit to each of the three components of the position time-series (i.e., east-west, north-south, up-down) has the form:

$$y(t) = y(t_0) + v(t - t_0) + \sum_{j=1}^{2} A_j \sin\left(j2\pi(t - t_0) + \phi_j\right) + \sum_{i=1}^{N} B_i H(t - T_i) + \sum_{k=1}^{M} C_k\left(1 - e^{(T_k - t)/\tau}\right) \quad (2)$$

where t is assumed to be in decimal years. $y(t_0)$ is the initial position at time t_0, and v is the slope (i.e., linear-trend or velocity). A_j and ϕ_j are the amplitude and phase of two periodic functions, where $j = 1$ and $j = 2$ represent an annual and semi-annual period, respectively. B_i and T_i are the amplitude and epoch of the ith of N offsets, and H is a Heaviside step function (i.e., $H = 0$ for $t < T_i$ and $H = 1$ for $t \geq T_i$). C_k and T_k are the amplitude and "decay" (or "relaxation") time, respectively, of a decay function describing postseismic deformation, here expressed as an exponential function describing decay after earthquake k at epoch T_k. The decay function can also be expressed as

15252027, 2024, 7, Downloaded from https://agupubs.onlinelibrary.wiley.com/doi/10.1029/2024GC011567, Wiley Online Library on [16/07/2024]. See the Terms and Conditions (https://onlinelibrary.wiley.com/terms-and-conditions) on Wiley Online Library for rules of use; OA articles are governed by the applicable Creative Commons License

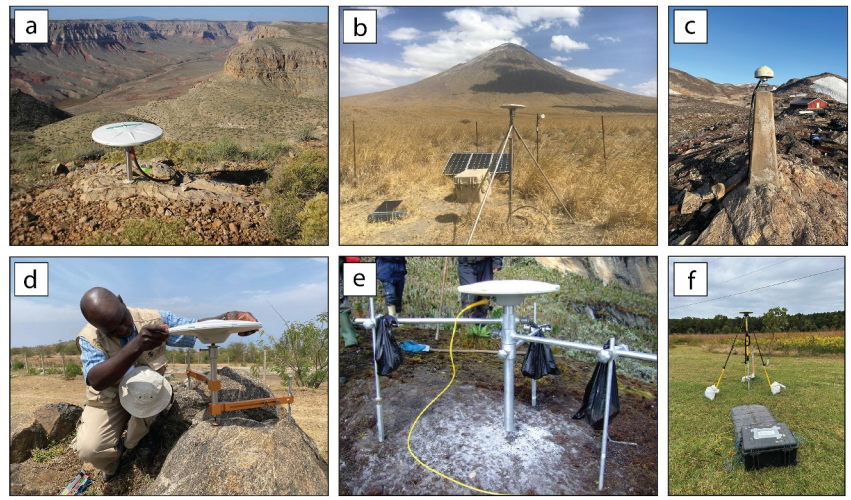

Figure 2. (a–c) Examples of semi-continuous or continuous Global Navigation Satellite System (cGNSS) station monumentation styles. (d–f) Examples of episodic GNSS (eGNSS) antenna mount styles. (a) Semi-continuous GNSS station SUNS in the United States with steel posts in bedrock monumentation. (b) cGNSS station OLO6 in Tanzania with shallow (~5 m) non-drilled braced monumentation in volcanic ash. (c) cGNSS station SCOR in Greenland with concrete pillar monumentation. (d) eGNSS station HYDP in Uganda with a bipod style antenna mount being set-up by geophysicist Joseph Nyago of the Uganda Ministry of Energy and Mineral Resources. (e) eGNSS site FFPS in Uganda with a tripod style antenna mount designed by Eric Calais. (f) eGNSS site VCR1 in the United States with a tripod style antenna mount. Photo credits: (a) C. Kreemer, (b, d–f) D. S. Stamps, (c) igs.org.

a logarithmic decay ($\log(1 + (t - T_k)/\tau)$, and is even occasionally modeled with cubic polynomials (Pollitz, 2015). The way the periodic function is expressed in Equation 2 cannot be solved with a least-squares linear regression. Therefore, in practice, the trigonometric function in (Equation 2) is expressed as

$$G_j \sin(j2\pi(t - t_0)) + F_j \cos(j2\pi(t - t_0)), \text{such that } A_j = \sqrt{(G_j^2 + F_j^2)}, \text{and } \phi_j = \tan^{-1}(F_j/G_j) \quad (3)$$

Time-series are typically presented in the reference frame in which the positions were estimated. This frame is normally a version of the ITRF. That frame's origin is defined as the center of the mass of the Earth's entire system (i.e., solid Earth plus fluids like ocean and atmosphere), and any vertically inferred velocity is relative to that frame. Sometimes, horizontal time-series are given relative to a stable tectonic plate. The defined reference frame will not affect any of the estimated parameters except the velocity.

The application of Equation 2 works best on time-series from cGNSS stations. For data from eGNSS campaign sites, the seasonal component is typically omitted. To minimize the seasonal effect on the estimation of the velocity, it is recommended that the eGNSS campaign measurements occur on the same days of each year such that the same seasonal signal is captured unless the seasonal component can be removed using a model. Either way, for eGNSS campaign time-series, Equation 2 typically reduces to just an initial position and a velocity estimation.

Figure 3 shows an example position time-series and superimposed station motion model for station SDWN in Myanmar (Lindsey et al., 2023). In this case, the position time-series is in the IGS14 reference frame, which implies ~29 and ~6 mm/yr velocity in the east and northward directions, respectively. This station was affected by the M6.8 Thabeikkyin earthquake on 11 November 2012, 52 km away from the station. The earthquake caused a considerable coseismic displacement in all three components and a postseismic decay is notable in the horizontal components. The vertical component contains a strong seasonal oscillation (likely reflecting loading at the Earth's surface of rainwater during the Southeast Asia monsoon). The seasonal signal is not a single sinusoid and is modeled by using a combination of an annual and semi-annual periodic function.

3.1. Coseismic or Other Offsets

Offsets in GNSS time-series typically have two causes: equipment changes or coseismic offsets from nearby earthquakes. Not estimating offsets present in the time-series has consequences for the estimation of other

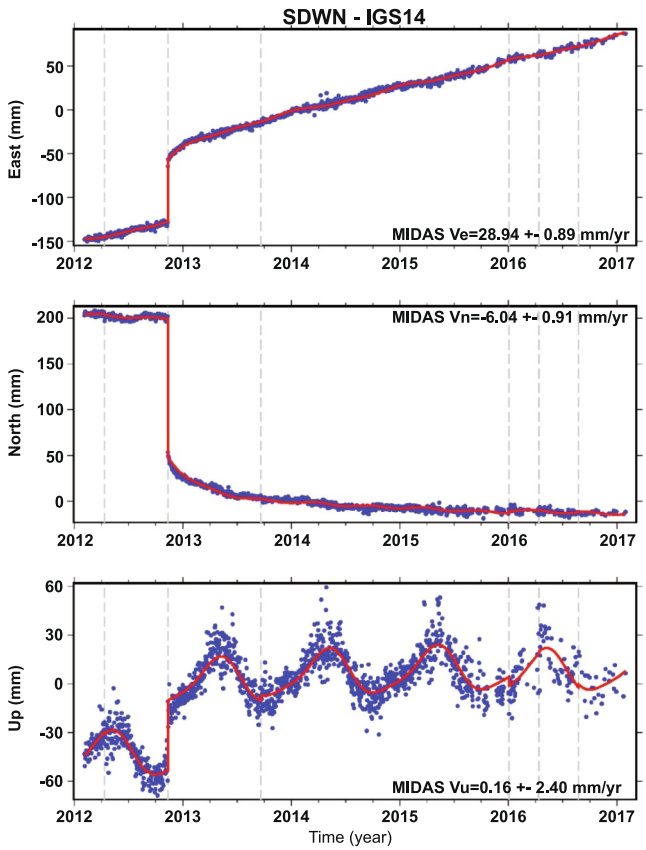

Figure 3. Example position time-series of 24-hr solutions using final orbits (blue dots) and station motion model (red line) for station SDWN in Myanmar (Lindsey et al., 2023) with the last day of data from 29 January 2017. Source: Nevada Geodetic Laboratory (Blewitt et al., 2018).

parameters, notably the velocity (Gazeaux et al., 2013; Griffiths & Ray, 2016; Tregoning et al., 2013; S. D. P. Williams, 2003). Offset detection and estimation is therefore critical because velocities are the founding data input to plate motion and strain rate estimation and are essential in maintaining stable reference frames.

Not all epochs with offsets have a known cause, such as a logged equipment change or the occurrence of a nearby earthquake. The reason for such an offset can be that no metadata is available for the station, or the metadata is not complete or erroneous. It is therefore important to manually screen the time-series. However, with the proliferation of GNSS time-series, automatic offset detection methods are being developed (Blewitt et al., 2013; Crocetti et al., 2021; Khazraei & Amiri-Simkooei, 2021; Lahtinen et al., 2021; D. Wu et al., 2018).

As an alternative to estimating the offset from a station motion model (Equation 2), in some instances (e.g., when the time-series are very short), coseismic offsets are estimated by comparing the average position for a set of days before an earthquake with those after the event. The disadvantage of this approach is that there can be a rapid postseismic transient (i.e., afterslip), which would bias this type of coseismic offset estimation. Also, this approach does not account for any of the noise content in the time-series, which affects the offset estimation (S. D. P. Williams, 2003).

Time-series from campaign measurements are less ideal for estimating coseismic offsets because any non-observed rapid postseismic decay likely will be lumped in with the actual coseismic offset to give a biased estimate of the true coseismic offset.

3.2. Postseismic Decay

As mentioned above, the postseismic decay in GNSS time-series is described by using either an exponential function, a logarithmic function, or a combination of the two. Therefore, if postseismic decay is being modeled, and the decay time is unknown, Equation 2 needs to be solved by using a non-linear regression method. It is also worth noting that for some earthquakes, it has been found that a combination of up to three decay functions is required to accurately model the total postseismic period (Ergintav et al., 2009; Tobita, 2016). These decay functions each have their own decay time and amplitude. Rather than estimating the decay function, other studies simply omit the postseismic period in their analysis and only solve for a combined co- and postseismic offset. However, this approach is correct only if after the exclusion time, the time-series has the same trend as before the earthquake.

3.3. Long-Term Trends—Velocities

The slope in the time-series can typically be interpreted as the long-term trend, or velocity, in the reference frame in which the position estimates are given. A least-squares fit to (2) would yield a velocity, albeit with a highly underestimated uncertainty due to the presence of time-correlated noise (see Section 3.5).

Some of the standard research-grade processing software packages such as GAMIT-GLOBK (Herring et al., 2018) and Bernese (Dach et al., 2015) have modules to estimate velocities, and GAMIT-GLOBK accounts for the time-correlated noise in the velocity uncertainty estimation (Herring, 2003; Reilinger et al., 2006). CATREF can be used to estimate velocities from a station network solution (used in the definition of the ITRF) (Altamimi et al., 2006). For estimating velocities from individual time-series, there are multiple algorithms/software packages: CATS (S. D. P. Williams, 2008), HECTOR (M. S. Bos et al., 2013), est_noise (Langbein, 2017), MIDAS (Blewitt et al., 2016). CATS, HECTOR, and est_noise allow the user to set and/or solve for the noise content in the time-series and produce a velocity uncertainty that accounts for the implied colored (i.e., time-dependent) noise (see Section 3.5). MIDAS makes no assumption of the noise content, and instead derives the velocity uncertainty from the median absolute deviation from a set of trends between positions 1 year apart,

15252027, 2024, 7, Downloaded from https://agupubs.onlinelibrary.wiley.com/doi/10.1029/2024GC011567, Wiley Online Library on [16/07/2024]. See the Terms and Conditions (https://onlinelibrary.wiley.com/terms-and-conditions) on Wiley Online Library for rules of use; OA articles are governed by the applicable Creative Commons License

15252027, 2024, 7, Downloaded from https://agupubs.onlinelibrary.wiley.com/doi/10.1029/2024GC011567, Wiley Online Library on [16/07/2024]. See the Terms and Conditions (https://onlinelibrary.wiley.com/terms-and-conditions) on Wiley Online Library for rules of use; OA articles are governed by the applicable Creative Commons License

where the velocity itself is the median of all trends of positions 1 year apart (see Blewitt et al. (2016) for details). Most studies have found that MIDAS-derived velocity uncertainties are slightly larger than those derived from stochastic models incorporating colored noise (Murray et al., 2019; Santamaría-Gómez et al., 2017; Simon et al., 2018), although Langbein (2020) found that they actually do not fully capture the rate uncertainties. Kreemer and Blewitt (2021) found that the precision in the MIDAS velocity captures the velocity accuracy, defined as the true temporal variability in the velocity.

3.4. Seasonal and Other Periodic Signals

While it is most common to estimate the seasonal variation with both an annual and semi-annual seasonal term in the station motion model, in some cases only an annual term is estimated. If the trend is the term of interest, then it is permissible to omit the seasonal terms when the time-series is >4.5 years long, because the influence of the seasonal terms on the trend estimation is negligible (Blewitt & Lavallée, 2002), although doing so may result in an overestimation of the noise level. If the time-series are <4.5 years long, the trend and seasonal terms should always be estimated simultaneously, and the estimation of a trend in the presence of seasonal terms should be altogether avoided for time-series <2.5 years because the correlation between the trend and seasonal terms becomes too large (Blewitt & Lavallée, 2002). The latter is the reason why most lithospheric studies focused on GNSS velocities adopt a minimum time-span of 2.5 years.

In the station motion model (Equation 2), it is assumed that the amplitude of the seasonal terms is constant with time. However, this assumption is valid only for first-order models, particularly because the main driver of seasonal variation is caused by hydrologic and atmospheric pressure loading. Ignoring the temporal variation could result in a seasonal signal remaining in the residual or seasonal time-series, and this signal could be completely out-of-phase from the original signal. Various methods have been proposed to account for the temporal variability in the periodic terms (Agnieszka & Dawid, 2022; Bennett, 2008; Q. Chen et al., 2013; Davis et al., 2012; Koulali & Clarke, 2021). Which method works best depends on the noise content in the time-series (see Section 3.5) (Klos et al., 2017).

A seasonal signal is the most prominent periodic signal to be found in the GNSS time-series, but other periodic signals exist as well. This does not apply to periodic signals associated with solid Earth and oceanic tides, which have already been accounted for at the processing level (although some studies have actually modeled those signals to learn more about upper mantle density and elastic moduli structure (see Section 6)). One known periodic signal is related to the GPS draconitic year (≈351.6 days or 1.04 cycles per year), which is the period at which the orientation of the GPS constellation repeats with respect to the Sun and this periodic signal is likely an artifact of mismodeled solar radiation pressure on GNSS satellites (Ray et al., 2008). Because this period is close to a year, it is absorbed in the seasonal signal estimation.

3.5. Noise in the Time-Series

The noise in the GNSS position time-series is not Gaussian, and for most stations consists of a combination of white noise and flicker noise (Amiri-Simkooei et al., 2007; Mao et al., 1999; Santamaría-Gómez et al., 2011; S. D. P. Williams et al., 2004). This temporally correlated noise causes the velocity uncertainty to be considerably (i.e., up to a factor of ∼10) larger than what a simple least-squares regression that assumes the data to be independent and identically distributed would give.

A large part of the flicker noise appears to originate from modeling errors of the orbits of GNSS (particularly GPS) satellites (Ait-Lakbir et al., 2023; King & Watson, 2010). Consequently, the time-series noise is correlated over large distances (Bogusz et al., 2015; D. Dong et al., 2006; Kreemer & Blewitt, 2021; Márquez-Azúa & DeMets, 2003; Y. Shen et al., 2014; W. Wang et al., 2019; S. D. P. Williams et al., 2004). This spatial correlation is enhanced by large-scale loading resulting from several processes such as hydrological droughts and atmospheric loading. The spatially correlated noise can be removed by stacking and removing the daily residual positions (Blewitt et al., 2013; Bogusz et al., 2015; Devoti et al., 2017; Kreemer & Blewitt, 2021; Márquez-Azúa & DeMets, 2003; Nikolaidis, 2002; Tian & Shen, 2016; Wdowinski et al., 1997). After this "filtering" of the time-series, the flicker noise component is indeed significantly reduced (W. Wang et al., 2019; S. D. P. Williams et al., 2004) and consequently the velocity uncertainty as well (Kreemer & Blewitt, 2021).

15252027, 2024, 7, Downloaded from https://agupubs.onlinelibrary.wiley.com/doi/10.1029/2024GC011567, Wiley Online Library on [16/07/2024]. See the Terms and Conditions (https://onlinelibrary.wiley.com/terms-and-conditions) on Wiley Online Library for rules of use; OA articles are governed by the applicable Creative Commons License

3.6. Time-Series Corrections

As the geodetic community has started to recognize the potential error sources in GNSS position time-series, some corrections are now being made available for the GNSS stations processed by the Nevada Geodetic Laboratory (NGL). The corrections consist of predicted displacements due to the elastic response to (a) non-tidal atmospheric loading (NTAL), (b) non-tidal oceanic loading, (c) loading from surface water and soil moisture, and (d) loading from any mass changes derived from the Gravity Recovery and Climate Experiment (GRACE and GRACE-FO) satellites. When these corrections are applied, the scatter in the residual time-series is typically significantly reduced. For example, Martens et al. (2020) found a reduction of 5%–30% by removing the effect of NTAL from time-series in the U.S. (in the vertical component). Such improvements in the scatter in the residual time-series affect the assessment of noise properties in the time-series (Gobron et al., 2021; Klos et al., 2021; Q. Wu et al., 2023) and thus also the uncertainty in the velocity estimate. Moreover, these corrections, particularly those from GRACE-derived loading, will affect the estimation of seasonal parameters (He et al., 2015).

Instead of correcting the time-series from the aforementioned loading sources, the time-series can also be filtered for common-mode noise, as described in Section 3.5. It has been found that filtering can reduce the noise more than the loading correction can (He et al., 2015; J. Yan et al., 2019), suggesting that loading models can be improved and other noise sources affecting large areas (e.g., orbital errors) are present in the GNSS time-series.

4. Applications of Secular Velocities

Secular GNSS velocities are long-term, steady surface motions that are typically aligned with the long-term, linear trend in daily position time-series (see Section 3.3). In this section, we describe a few applications of secular velocities with a focus on lithospheric studies.

4.1. Plate Motions and Deformation Zones

Secular GNSS velocities can be used to test for and constrain rigid plate (or block) motions using both inverse and forward modeling numerical approaches. Here, we assume a plate is lithospheric, but a block can be crustal or lithospheric depending on its thickness. Inverting secular GNSS velocities for a rigid body rotation, which can be done with kinematic modeling codes, such as TDEFNODE (McCaffrey, 2009) and Blocks (Meade & Loveless, 2009), and testing for plate rigidity is a common approach for resolving block/plate geometries, angular rotations of plate motions, and zones of deformation (e.g., J. Elliott & Freymueller, 2020; Meade & Hager, 2005; Stamps et al., 2021; Wallace et al., 2004). Forwarding modeling approaches that produce estimates of surface motions, such as thin-sheet modeling (i.e., Bird & Piper, 1980; England & McKenzie, 1982; Flesch et al., 2001; Haines & Holt, 1993) or 3D finite element modeling (i.e., Heister et al., 2017; Kronbichler et al., 2012; Moresi et al., 2014), can also be used to investigate lithospheric dynamics through comparisons with GNSS velocities or predicted plate motions from kinematic models.

Prior to broadscale availability of GNSS data, inverse kinematic models used to estimate global plate motions were first constrained by transform azimuths and spreading rate data (Le Pichon, 1968) with earthquake slip vectors incorporated later (Chase, 1972, 1978; DeMets et al., 1990; Minster & Jordan, 1978). Historically, comparisons of plate models constrained by geologic data (transform azimuths, earthquake slip vectors, and spreading rate data) and early geodetic data (Very Long Baseline Interferometry and Satellite Laser Ranging observations) revealed steady interior plate motions for at least 3 million years (e.g., Argus & Gordon, 1990; Gordon, 1991; Robbins et al., 1993). The advancement of using GNSS data over geologic data is that a number of plates in a geologic plate motion model have their motion indirectly estimated on the basis of plate circuit closures, while direct geodetic estimation can be done for any plate with velocity observations at least two distinct locations. Moreover, there are some examples where it appears that plate motion has systematically been changing over recent geologic times, such as the slow-down of the Nazca-South America convergence rate (e.g., Norabuena et al., 1999). The latest GNSS based plate motion models are GEODVEL (Argus et al., 2010), GSRM v2.1 (Kreemer et al., 2014), NCL20 (Vardić et al., 2022), and the ITRF2020 plate model (Altamimi et al., 2023). The differences between these models arise from the amount of station velocities considered, number of plates covered, if and how GIA corrections have been made, whether interplate deforming zones are considered, and also whether a translation rate of the Earth's center (i.e., the origin of the Cartesian reference frame) is included.

15252027, 2024, 7, Downloaded from https://agupubs.onlinelibrary.wiley.com/doi/10.1029/2024GC011567, Wiley Online Library on [16/07/2024]. See the Terms and Conditions (https://onlinelibrary.wiley.com/terms-and-conditions) on Wiley Online Library for rules of use; OA articles are governed by the applicable Creative Commons License

From a forward modeling perspective, the balance of forces driving surface motions and physical properties of the lithosphere-convecting mantle system can be investigated through comparisons of modeled surface velocities with observed GNSS velocities that represent the same timescale of the model or predicted velocities from kinematic models such as GEODVEL. The physical set-ups of forward models can be constrained by a wide range of observations and models, such as seismic velocity models, fault geometries, subduction models, gravity, experimental observations for material parameters, crustal thickness models, lithospheric thickness models, and tectonic plate or block geometries. Extensive forward modeling studies have investigated the relative roles of plate driving forces with different assumptions at the global scale (i.e., Becker, 2006; Becker & O'Connell, 2001; Bird, 1998; Bird et al., 2008; Conrad & Lithgow-Bertelloni, 2002; Ghosh & Holt, 2012; Ghosh, Becker, & Humphreys, 2013; Ghosh, Holt, & Wen, 2013; Saxena et al., 2023; Zhong, 2001) and regional scale (i.e., England & Molnar, 1997; Finzel et al., 2015; Flesch et al., 2007; Liu & King, 2022; Rajaonarison et al., 2021, 2023; Stamps et al., 2014, 2015; Vergnolle et al., 2007), often finding contradictory results.

As more high-precision GNSS data have become available, the stability and geometry of plate interiors have been reassessed. For example, the geometry of the Nubian-Somalian plate system (formerly the African plate) has been greatly revised to include at least three microplates (Victoria, Rovuma, Lwandle) and a broad deforming zone since the early 2000s in light of new geologic data from along the Southwest Indian Spreading Ridge (e.g., Horner-Johnson et al., 2007) and new GNSS observations along the East African Rift System (Calais et al., 2006; Fernandes et al., 2013; Saria et al., 2014; Stamps et al., 2008, 2021). Furthermore, the stability of the Nubian plate has been challenged. Using 133 GNSS stations and 9 DORIS (Doppler Orbitography by Radiopositioning Integrated on Satellite) stations across the continent of Africa, the Nubian plate was found to be rigid with a root mean square residual of 0.6 mm/yr (Saria et al., 2013) with a follow-up geodetic study by Njoroge et al. (2017) confirming Nubian plate rigidity. Yet, a few years later, Wedmore et al. (2021) used more GNSS data and resolved the distinctly rotating San microplate in southern Africa. In another case, the North American plate was found to be slowly deforming in response to GIA based on an analysis of 3,271 GNSS stations (Kreemer et al., 2018). These examples demonstrate the capabilities of having a denser distribution of high precision GNSS secular velocities available for studies of the lithosphere.

4.2. Strain Rates

GNSS velocity fields can be powerful tools in elucidating the regional tectonics or even geodynamic driving forces, but only when the velocity field is presented in an appropriate reference frame (e.g., Kreemer & Chamot-Rooke, 2004; Wdowinski et al., 2007; G. Zhao et al., 2022). On the other hand, when presented in an inappropriate reference frame, velocity fields can obscure the regional tectonic signal. Because the underlying deformation field is the same regardless of the reference frame in which the velocities are presented, strain rate tensor fields can be considered the more objective property to describe and evaluate localized deformation.

A field of GNSS-derived horizontal velocities can be expressed by an underlying velocity gradient tensor field (F). If the GNSS stations are located in an area of deformation (as opposed to being on a rigid plate or block), F can be decomposed into a 2D strain rate tensor and rotation rate vector component. There are multiple proposed methods to derive a strain rate tensor field, varying from using wavelets (Su et al., 2019; Tape et al., 2009; K. Xu et al., 2020), the least-squares collocation method (Caporali et al., 2003; El-Fiky & Kato, 1998; Kahle et al., 1995; Y. Wu et al., 2011), weighted least-squares regression (Z.-K. Shen et al., 1996, 2007, 2015), spline fitting (Beavan & Haines, 2001; Hackl et al., 2009), elasticity theory (Haines et al., 2015; Noda & Matsu'ura, 2010; Sandwell & Wessel, 2016), Bayesian estimation (Pagani et al., 2021; Xiong et al., 2021), basis function expansion (Okazaki et al., 2021), and robust imaging (Kreemer et al., 2018, 2020). Many software packages that derive strain rates are publicly available (Cardozo & Allmendinger, 2009; Goudarzi et al., 2015; Materna et al., 2021; Pietrantonio & Riguzzi, 2004; Ramírez-Zelaya et al., 2023; Sandwell & Wessel, 2016; Z.-K. Shen et al., 2015; Teza et al., 2023). Note that not all methods and packages use spherical geometry to estimate strain rates.

In areas of known large fault systems, the strain rate is often assumed to reflect elastic strain accumulation that will convert into permanent deformation on a fault during an earthquake. In particular, the elastic strain rate is expected to localize above major faults (i.e., dislocations) when they are locked in the seismogenic crust but slip continuously along their down-dip continuation (Savage & Burford, 1973). Alternatively, instead of having discrete strike-slip faults, shear might be distributed over a finite zone below the seismogenic crust, which would be expressed as a zone of constant shear strain rate in the elastic upper crust (Prescott & Nur, 1981). The strain rate

15252027, 2024, 7, Downloaded from https://agupubs.onlinelibrary.wiley.com/doi/10.1029/2024GC011567, Wiley Online Library on [16/07/2024]. See the Terms and Conditions (https://onlinelibrary.wiley.com/terms-and-conditions) on Wiley Online Library for rules of use; OA articles are governed by the applicable Creative Commons License

pattern can thus reveal whether faults continue as discrete planes into the ductile lower crust; however, a dense GNSS network is required to make this determination. For most major strike-slip boundaries, the GNSS data are consistent with the dislocation model (Vernant, 2015 and ref. therein). More generally, the elastic dislocation principle is used to infer the slip rate of the creeping dislocation in the lower crust, which is understood to be the long-term fault slip rate. When the strain rate field is determined for an area, it is generally implied that the area is deforming in a spatially continuous fashion. Indeed, while some major faults or plate boundaries are readily revealed by localized strain rates, for many other areas the strain rates are diffusely distributed (e.g., D'Agostino et al., 2020; Hao et al., 2019; Kreemer & Young, 2022; Kreemer et al., 2014; Métois et al., 2015; Pagani et al., 2021; Rui & Stamps, 2019; Stevens & Avouac, 2021; M. Wang & Shen, 2020; Xiang et al., 2021). Such results support the interpretation of a strain rate field in terms of a thin-sheet approximation of the lithosphere. Some studies have considered the strain rate tensor (and the implied style and orientation of deformation) as a proxy for the stress tensor and used strain rate models for plate boundary zones to calibrate the contribution of the various forces acting on the lithosphere, such as boundary forces, basal tractions, and gravitational potential energy (e.g., Flesch & Kreemer, 2010; Flesch et al., 2000; Ghosh et al., 2006; Özeren & Holt, 2010; Stamps et al., 2014).

In a different approach, spatial variations in strain rates have been interpreted to be the result of lateral variations in elastic plate thickness (Chéry, 2008; Traoré et al., 2014) or, more generally, effective lithospheric rigidity (Chéry et al., 2011; Furst et al., 2018). Other studies have focused on constraining rigidity (as well as viscosity) contrasts across major (strike-slip) faults from an observed asymmetry of elastic strain accumulation with respect to the surface fault trace (e.g., Ge et al., 2022; Houlié & Romanowicz, 2011; W.-J. Huang & Johnson, 2012; Jolivet et al., 2009; Le Pichon et al., 2005; Schmalzle et al., 2006). However, it has been shown that the observed asymmetry can also be reproduced by a contrast in the thickness of the elastic layer (e.g., Vaghri & Hearn, 2012) or a non-vertical fault dip (e.g., A. G. Bos et al., 2004).

5. Applications of the Postseismic Decay Signal

Non-linear postseismic decay signals can be detected by GNSS stations days to years after a major earthquake. The physical processes that drive postseismic deformation detected in GNSS time-series are typically attributed to afterslip, poroelastic effects, and viscoelastic relaxation in the lower crustal and/or upper mantle (e.g., Hearn, 2003; Bürgmann & Dresen, 2008 and ref. therein). One can characterize a postseismic decay signal in position time-series data by using a logarithmic function that can explain afterslip (Marone et al., 1991) and/or an exponential function to characterize viscoelastic relaxation (Savage & Prescott, 1978). Both the logarithmic and exponential functions provide constraints on the amplitude and duration of transient signals. In some cases, time-series data with postseismic decay signatures can be represented by both a logarithmic decay function days after the main event in response to afterslip with longer term signals due to a relaxation mechanism represented by an additional exponential function. Temporal constraints on the postseismic decay signal allow for the construction of cumulative postseismic displacements (e.g., Freed et al., 2006; Rui & Stamps, 2016); thus, one can use such displacements to investigate the physics underlying postseismic processes using numerical models. However, there is often debate over which process or processes (i.e., afterslip, poroelastic effects, and viscoelastic relaxation) cause the postseismic signals because of the non-uniqueness in fitting the time-series data (e.g., Sobrero et al., 2020). In Sections 5.1–5.3 we provide information about how postseismic decay signals can be used to investigate afterslip, poroelasticity, and rheology in the crust and upper mantle.

5.1. Afterslip

Large earthquakes create stress changes that can cause transient slip on the fault that ruptured well after the main event occurred, known as afterslip. Afterslip can occur above, below, or along the seismogenic rupture zone and is governed by the temperature-dependent frictional properties of the faulted system (e.g., Segall, 2010; Figure 1). The 1966 Parkfield, California earthquake was the first seismic event that had an observable afterslip in creepmeter data (Smith & Wyss, 1968). Numerous subsequent earthquakes observed with GNSS stations have exhibited afterslip signals in GNSS time-series that are fit with a logarithmic function (see Section 5) such as the 1994 M6.7 Northridge, California event (Donnellan & Lyzenga, 1998), the 1999 M7.4 Izmit, Turkey event (Özarpaci et al., 2021), and the M7.3 9 March 2011 foreshock to the major Tohoku, Japan earthquake (Ohta et al., 2012). Using a kinematic afterslip model that fits GNSS time-series data, one can use the steady-state

15252027, 2024, 7, Downloaded from https://agupubs.onlinelibrary.wiley.com/doi/10.1029/2024GC011567, Wiley Online Library on [16/07/2024]. See the Terms and Conditions (https://onlinelibrary.wiley.com/terms-and-conditions) on Wiley Online Library for rules of use; OA articles are governed by the applicable Creative Commons License

frictional sliding theory (e.g., Scholz, 1998) to estimate fault friction properties (e.g., Liu-Zeng et al., 2020; Perfettini & Avouac, 2004), although caution must be taken due to parameter trade-offs.

5.2. Poroelastic Effects

Numerous processes associated with the lithosphere can be investigated assuming simplified material properties, such as a homogeneous elastic crust. However, the crust is actually porous and contains regions of partial saturation that result in poroelastic mechanical behavior (Segall, 2010). Strain impacts fluid pressure; thus, the crust responds when there are changes in subsurface water volumes. For example, Abidin et al. (2008) constrained 1–10 cm/yr of land subsidence in Jakarta, Indonesia using campaign GNSS observations (1997–2005) and attributed the deformation to excessive groundwater extraction. Assuming certain mechanical properties of the upper crust, numerous studies have investigated the properties of aquifers using GNSS observations of vertical land motions (e.g., Argus, Fu, & Landerer, 2014; Argus, Peltier, et al., 2014; Biessy et al., 2011; D'Agostino et al., 2018; Silverii et al., 2016). In addition, poroelastic deformation has been detected in GNSS time-series after several seismic events because changes in coseismic stress affect volumetric crustal strain. For example, Decriem and Árnadóttir (2012) observed poroelastic rebound/relaxation signals in a GNSS time-series that had an opposite sense of motion to the coseismic signal after two M6 events in the South Iceland Seismic Zone that occurred on 29 May 2008. In another case, Freed et al. (2006) used numerical modeling that incorporated poroelastic effects to fit postseismic GNSS time-series and velocities that captured the 2002 Denali, Alaska earthquake and inferred information about upper mantle rheology.

5.3. Rheology

Postseismic decay signals from GNSS data can be used to estimate the rheological properties of ductile crustal regimes and the upper mantle (lithospheric mantle and upper asthenosphere), assuming time-dependent visco-elastic behavior. Representative Maxwell and biviscous Burgers constitutive equations of linear elastic and linear viscous behavior are commonly used to approximate the values of viscosity in the ductile crust and upper mantle (e.g., Bürgmann & Dresen, 2008; M. H. Huang et al., 2014; K. Wang et al., 2012). In addition to the Maxwell and Burgers models, more realistic power-law constitutive equations for ductile flow and dislocation creep deformation constrained by laboratory experiments (e.g., Hirth & Kohlstedf, 2003) can be used to determine material properties that best-fit postseismic decay signals. For example, Freed and Bürgmann (2004) constrained the material parameter $n = 3.5$ for a non-linear power-law rheology of the upper mantle in southern California using forward models and fitting to postseismic GNSS time-series and displacements associated with the 1992 Landers and 1999 Hector Mines earthquakes. In some instances, a viscosity contrast in the lower crust across a ruptured fault has been required to explain an asymmetric postseismic deformation pattern observed by GNSS (e.g., Liu et al., 2019).

6. Seasonal and Other Periodic Loading

A load on the Earth's surface will deform the surface in three dimensions. Half-space models as well as spherical layered models have been proposed to relate the load to the resulting elastic deformation, but only the spherical models (e.g., LoadDef (Martens et al., 2019) based on the work of Farrell (1972)) give correct results (Argus et al., 2017; Chanard et al., 2014). Because there is a trade-off between long-term (un)loading and the long-term trend related to tectonics, periodic signals are the most suitable to investigate the relationship between the load and the observed deformation. It is also found that both horizontal and vertical data should be considered to better understand the load and the elastic structure (Chanard et al., 2014; Milliner et al., 2018; Silverii et al., 2016; Wahr et al., 2013; You & Yuan, 2021).

Up to 50% of the observed seasonal signal can be explained by stress imposed onto the Earth's surface from the annual redistribution of various mass loading sources in the hydrosphere, atmosphere, cryosphere, and ocean (e.g., Chanard, Fleitout, Calais, Rebischung, & Avouac, 2018; D. Dong et al., 2002; Jiang et al., 2013). Some of the remainder of the signal can be attributed to thermo-elastic effects (Fang et al., 2014; Prawirodirdjo et al., 2006; Romagnoli et al., 2003; Tsai, 2011; X. Xu et al., 2017; H. Yan et al., 2009), the aforementioned draconitic period, and pole tide (i.e., a solid Earth tide that is the result of the annual wobble of Earth's axis) (D. Dong et al., 2002), while a significant part remains unexplained. As a result, caution should be taken when interpreting the seasonal component in GNSS time-series in terms of the contributing loading source and, particularly, the response of the

15252027, 2024, 7, Downloaded from https://agupubs.onlinelibrary.wiley.com/doi/10.1029/2024GC011567, Wiley Online Library on [16/07/2024]. See the Terms and Conditions (https://onlinelibrary.wiley.com/terms-and-conditions) on Wiley Online Library for rules of use; OA articles are governed by the applicable Creative Commons License

solid Earth (Chanard et al., 2020). Still, some advances have been made in constraining Earth's (an)elastic structure by comparing the observed seasonal displacements with those predicted from a surface load derived from data from, for example, GRACE. For example, Chanard et al. (2014) found that the GNSS seasonal signal in the Himalayas fits better when lowering the crustal density given by the PREM model. Drouin et al. (2016) found a lower rigidity underneath Iceland compared to the global PREM average. Chanard, Fleitout, Calais, Barbot, and Avouac (2018) found that the transient asthenospheric viscosity cannot be lower than 5×10^{17} Pa s.

To avoid having to assume that all of the seasonal deformation is induced by seasonal surface loading, one can use the periodic signals that are associated with either the solid Earth tide or with the well-known OTL. While those signals are typically accounted for at the processing level, some studies have tested whether variation of the (an)elastic structure of the upper mantle would yield a better data fit. Ito and Simons (2011) studied the OTL response in the western U.S. and found that the 220 km (Lehmann) discontinuity in PREM is not present there and that there exists a low-density anomaly of ~50 kg/m^3 between 80 and 250 km depth. Other studies explained required deviations from using PREM as there being a component of anelasticity in the asthenosphere globally (Kang et al., 2015) as well as specifically underneath Europe (M. S. Bos et al., 2015), the South China Sea (J. Wang et al., 2020), and the Canary Islands (Arnoso et al., 2023). Lateral variations in elastic structure were suggested to explain OTL misfit for South America (Martens et al., 2016), Alaska (Martens & Simons, 2020), and New Zealand (Matviichuk et al., 2021).

7. Applications of Coseismic Displacements

The coseismic offsets represent the instantaneous release of elastic strain at the time of the earthquake. That strain had accumulated in the crust during the time the fault on which the earthquake occurred was locked in the "interseismic period." Most often the offsets are consistent with those predicted by a model of a slip on a dislocation in the elastic upper crust (Okada, 1985). The dislocation model is, in fact, used to infer the amount of (average) slip on one or more fault(s) with a given geometry (e.g., Banerjee et al., 2007; Hammond, Blewitt, Kreemer, Koehler, & Dee, 2021; Hunstad et al., 1999; C. R. Williams et al., 1993). When many GNSS stations are present in the near-field, the entire fault plane is often subdivided into many fault patches with which a detailed slip model can be derived (which typically involves some sort of inversion regularization) (e.g., Cheloni et al., 2010; Ching et al., 2007; Diao et al., 2011; Freymueller et al., 1994; Hreinsdóttir et al., 2003; Johanson et al., 2006; Kreemer, Blewitt, & Maerten, 2006; Ozawa et al., 2011; Reilinger et al., 2000). These slip models can be compared or integrated with those derived from other data.

For the largest earthquakes, such as the 2004 Great Sumatra and 2011 Tohoku earthquakes, coseismic offsets can be observed thousands of kilometers away (e.g., Banerjee et al., 2005; Kreemer, Blewitt, Hammond, & Plag, 2006; Tregoning et al., 2013; Vigny et al., 2005; W. Wang et al., 2014; B. Zhao et al., 2012). In those cases, the offsets can only be explained (e.g., Fu & Sun, 2006; Kreemer, Blewitt, Hammond, & Plag, 2006; Pollitz et al., 2011; W. Wang et al., 2014) by considering a spherical layered Earth model (Pollitz, 1996; Sun et al., 1996; R. Wang et al., 2006).

GNSS data have not only aided in understanding the earthquake process (and we are omitting here the contributions of high rate GNSS) but also in the associated 3D rigidity properties of the surrounding rock. First of all, it is important to include a realistic increase in the shear modulus with depth in order to best model the slip and depth extent of the rupture and to constrain the associated seismic moment, which otherwise would be underestimated (e.g., Hearn & Bürgmann, 2005; Kreemer, Blewitt, Hammond, & Plag, 2006). Second, similar to the interseismic strain accumulation, an asymmetry in strain release is expected when the fault plane separates distinctly different lithologies. However, any observed asymmetry in coseismic displacements on strike-slip faults is often interpreted by the fault having a slight dip (e.g., Yong-Ge et al., 2008).

8. Resources

To assist researchers seeking precision GNSS data for their studies of the lithosphere, in this final section we provide information about several locations where such appropriate open-access GNSS data and data products can be found.

15252027, 2024, 7, Downloaded from https://agupubs.onlinelibrary.wiley.com/doi/10.1029/2024GC011567, Wiley Online Library on [16/07/2024]. See the Terms and Conditions (https://onlinelibrary.wiley.com/terms-and-conditions) on Wiley Online Library for rules of use; OA articles are governed by the applicable Creative Commons License

8.1. GNSS Time-Series

GNSS position time-series can be accessed from several online sources in a variety of formats given that there is currently no agreed-upon standard for position time-series data. Below, we discuss daily position GNSS time-series data provided open access by NASA, the Geodetic Facility for the Advancement of Geoscience (GAGE) operated by the EarthScope Consortium, and the NGL. These three resources are described because they provide data for a wide range of stations rather than one specific locality.

NASA's archive for space geodetic data called the Crustal Dynamics Data Information System (CDDIS; Noll, 2010) provides daily position GNSS time-series data through the Making Earth Science Data Records for Use in Research Environments (MEaSUREs) Program. Users access the time-series data using a free account with the NASA EarthData Portal or through an anonymous ftp service via the Scripps Orbit and Permanent Array Center (SOPAC; ftp://garner.ucsd.edu/pub/timeseries/). MEaSUREs provides time-series produced by NASA's JPL and SOPAC. Several types of daily GNSS position time-series data are available, including but not limited to Raw, Cleaned, Trended, Detrended, and Residual data. Which GNSS time-series data should be used in lithospheric studies depends on the process(es) being investigated. More details about the MEaSUREs GNSS time-series data can be found at this link (https://cddis.nasa.gov/Data_and_Derived_Products/GNSS/MEaSUREs/gnss_measures_daily_displacement_timeseries_001.html).

The US National Science Foundation supported GAGE facility operated by the EarthScope Consortium provides daily position GNSS time-series data to registered users via an online archive, an Observable notebook, or through Web Services (see https://www.unavco.org/data/gps-gnss/gps-gnss.html for the three access methods). Three research groups produce "rapid" and "final" daily GNSS position time-series data: Central Washington University (cwu), New Mexico Tech (nmt), and the Massachusetts Institute of Technology (pbo). For lithospheric studies, a researcher should use the "final" version of the time-series data, which are based on positioning procedures that use precise final satellite orbits (see Section 2).

The NGL based at the University of Nevada, Reno and the Nevada Bureau of Mines and Geology processes over 21,000 continuous GNSS stations globally and provides daily position time-series data for each station in "rapid" and "final" versions (Blewitt et al., 2018). Similar to the GAGE products, "final" daily time-series data should be used in lithospheric studies. NGL provides their data in tenv3 (http://geodesy.unr.edu/gps_timeseries/README_tenv3.txt), tenv (http://geodesy.unr.edu/gps_timeseries/README_tenv.txt), and xyz (http://geodesy.unr.edu/gps_timeseries/README_txyz2.txt) formats. Users have the ability to download single files through station pages using websites (map link http://geodesy.unr.edu/NGLStationPages/gpsnetmap/GPSNetMap.html, station list link http://geodesy.unr.edu/NGLStationPages/GlobalStationList).

8.2. GNSS Velocities

Several organizations or facilities produce GNSS velocities (horizontal and vertical components) with 1-sigma uncertainties and make their solutions available online in an ascii or csv format. Here, we discuss GAGE (operated by the EarthScope Consortium) (Herring et al., 2016), NASA CDDIS via the MEaSUREs project (Bock et al., 2021), and NGL (Blewitt et al., 2018) for complete velocity solutions due to their ease of use and global coverage. GAGE provides velocity solutions produced by Central Washington University (cwu), New Mexico Tech (nmt), and the Massachusetts Institute of Technology (pbo) as well as a few velocity solutions associated with specific peer-reviewed research manuscripts (e.g., Rui & Stamps, 2019; Stamps et al., 2021) at this https://gage-data.earthscope.org/archive/gnss/products/velocity/ (EarthScope login required). Velocity solutions for individual continuous GNSS stations can also be accessed via EarthScope using web services without a login at https://www.unavco.org/data/web-services/documentation/documentation.html. The NASA MEaSUREs project provides their velocity solutions at https://cddis.nasa.gov/archive/GPS_Explorer/archive/velocities/V1/ in ascii format (NASA Earth Data login required). NGL regularly updates its velocity solution and provides the most recent version in an IGS14 reference at http://geodesy.unr.edu/velocities/midas.IGS14.txt with the format of the file described http://geodesy.unr.edu/velocities/midas.readme.txt. NGL velocity solutions in other reference frames are also available through their main website (http://geodesy.unr.edu/) under the section MIDAS Velocity Fields.

Partial velocity solutions with 1-sigma uncertainties in the vertical component only are also provided open access by the French organization Système d'Observation du Niveau des Eaux Littorales (SONEL). SONEL ingests

GNSS time-series data for mostly coastal GNSS stations from four sources (University of La Rochelle, NGL, JPL, and German Research Center for Geosciences) and provides a web interface (https://www.sonel.org/-Vertical-land-movements-.html?lang=en) for downloading an ascii file of the vertical velocity data.

8.3. Derived Products

A number of products derived from GNSS data are available from several online sources, of which we list a few here. EarthScope provides position offsets and events that may be useful for time-series analysis at this website (https://www.unavco.org/data/gps-gnss/gps-gnss.html) under Data Product Level 2. NGL has an interpolated vertical velocity product available (http://geodesy.unr.edu/vlm.php) based on the work of Hammond, Blewitt, Kreemer, and Nerem (2021). The NASA CDDIS MEaSURES project provides strain rate grids (https://cddis.nasa.gov/archive/GPS_Explorer/archive/strain_rate_grids/V1/) and transient signals from along the Cascadia subduction zone (https://cddis.nasa.gov/archive/GPS_Explorer/archive/transients/V1/).

8.4. GNSS RINEX Files

Below we provide links to a set of repositories that provide RINEX files of GNSS data that can be processed for one's own position and velocity solutions. We note that the International GNSS Service (IGS) provides a number of products that are useful when processing one's own solution (https://igs.org/products/). When available, we provide a link to a repository/network description website in addition to a data access link, however not all repositories provide both websites. Most repositories provide their RINEX files without needing an account; however, some do. While the majority of repositories listed below have moved away from using FTP services, a few still use FTP for file access that is noted below.

1. African Geodetic Reference Frame (AFREF): Description (https://rcmrd.org/en/apps-data/afref-and-geodesy) and data access (http://afrefdata.org/).
2. Argentina RAMSAC: Data description (https://www.ign.gob.ar/NuestrasActividades/Geodesia/Ramsac) and data access (https://wilkilen.fcaglp.unlp.edu.ar/gnss) (account needed).
3. Australia GNSS data center: Description (https://www.ga.gov.au/scientific-topics/positioning-navigation/geodesy/gnss-networks) and data access (https://ga-gnss-data-rinex-v1.s3.amazonaws.com/index.html).
4. Brasil RBMC: Description (https://www.ibge.gov.br/en/geosciences/geodetic-positioning/geodetic-networks/19213-brazilian-network-for-continuous-monitoring-of-the-gnss-systems.html) and data access (https://geoftp.ibge.gov.br/informacoes_sobre_posicionamento_geodesico/rbmc/).
5. British Columbia Active Control System: Description (https://www2.gov.bc.ca/gov/content/data/geographic-data-services/geo-spatial-referencing/bcacs) and data access (ftp://acs-ftp.gdbc.gov.bc.ca/RINEX).
6. Canadian Geodetic Survey: Data access (https://cacsa.nrcan.gc.ca/).
7. Canary Islands: Description (https://www.grafcan.es/servicios/red-estaciones-gnss/) and data access (https://gnss.grafcan.es/).
8. Chile—Centro Sismológical National: Description (http://gps.csn.uchile.cl/) and data access (http://gps.csn.uchile.cl/data/).
9. EarthScope Consortium, Inc.: Several data access methods (https://www.unavco.org/data/gps-gnss/gps-gnss.html).
10. European Plate Observing System: Description (https://www.epos-eu.org/tcs/gnss-data-and-products) and data access (https://datacenter.gnss-epos.eu/).
11. EUREF permanent GNSS network: Description (https://epncb.oma.be/) and data access (https://igs.bkg.bund.de/root_ftp/EUREF/ and http://epncb.oma.be/ftp/obs/).
12. France—RENAG: Description (https://renag.resif.fr/en/presentation/) and data access (ftp://renag.unice.fr/data/); Reseau GNSS Permanent: Description (https://rgp.ign.fr/) and data access (ftp://rgpdata.ign.fr/pub/data).
13. GFZ Information System and Data Center: Data access (ftp://isdcftp.gfz-potsdam.de/gnss/).
14. Greece NOANET: Description (http://geodesy.gein.noa.gr:8000/nginfo/) and data access (http://www.gein.noa.gr/services/GPSData/).
15. Greenland: Description (https://dataforsyningen.dk/data/4804) and data access (http://ftp.dataforsyningen.dk/GNSS).
16. Hartebeesthoek Radio Astronomy Observatory: Data access (http://geoid.hartrao.ac.za/archive/rinex/).

15252027, 2024, 7, Downloaded from https://agupubs.onlinelibrary.wiley.com/doi/10.1029/2024GC011567, Wiley Online Library on [16/07/2024]. See the Terms and Conditions (https://onlinelibrary.wiley.com/terms-and-conditions) on Wiley Online Library for rules of use; OA articles are governed by the applicable Creative Commons License

15252027, 2024, 7, Downloaded from https://agupubs.onlinelibrary.wiley.com/doi/10.1029/2024GC011567, Wiley Online Library on [16/07/2024]. See the Terms and Conditions (https://onlinelibrary.wiley.com/terms-and-conditions) on Wiley Online Library for rules of use; OA articles are governed by the applicable Creative Commons License

17. Hong Kong SatRef: Description (https://www.geodetic.gov.hk/en/satref/satref.htm) and data access (https://rinex.geodetic.gov.hk/).
18. Iceland—Icelandic Met Office data access (https://data.epos-iceland.is/files/gps/) and National Land Survey of Iceland data access (ftp://ftp.lmi.is/gnsmart_data/).
19. Italy—Italian Geodetic Data Archiving Facility (GeoDAF): Description (http://geodaf.mt.asi.it/) and data access (ftp://geodaf.mt.asi.it/GEOD/GPSD/RINEX/); Instituto Nationale di Geofisica e Volcanologia: Description (http://ring.gm.ingv.it/?page_id=702) and data access (ftp://gpsfree.gm.ingv.it/OUTGOING/RINEX30/RING/); Instituto Geografico Militare: Description (https://www.igmi.org/en/direzione-geodetica/progetto-rdn-rete-dinamica-nazionale) and data access (ftp://37.207.194.154/).
20. IGS and NASA Crustal Dynamics Data Information Center (CDDIS): Description (https://cddis.nasa.gov/Data_and_Derived_Products/GNSS/GNSS_data_holdings.html) and data access (https://cddis.nasa.gov/archive/gnss/data/daily), account needed.
21. Japan Aerospace Exploration Agency (JAXA): Data access (ftp://mgmds01.tksc.jaxa.jp/).
22. Japan GEONET: Description (https://www.gsi.go.jp/ENGLISH/geonet_english.html) and data access (ftp://terras.gsi.go.jp/data/) (account needed).
23. Mexico INEGI: Description (https://en.www.inegi.org.mx/temas/geodesia_activa/) and data access (ftp://geodesia.inegi.org.mx/home/rgna).
24. Nanyang Technological University: Access to data from different networks in Southeast Asia (ftp://data-collection.earthobservatory.sg/).
25. National Geodetic Survey CORS Network: Description (https://geodesy.noaa.gov/CORS/index.shtml) and data access (https://geodesy.noaa.gov/corsdata/rinex/).
26. New Zealand GeoNET: Description (https://www.geonet.org.nz/data/types/geodetic) and data access (https://data.geonet.org.nz/gnss/rinex/).
27. Northern California Earthquake Data Center: Description (https://www.ncedc.org/usgs-gps/) and data access (https://ncedc.org/gps/highrate/rinex/).
28. Pacific Northwest Geodetic Array: Description (https://www.geodesy.org/) and data access (https://www.panga.cwu.edu/pub/data/).
29. Panama—Description (https://ignpanama.anati.gob.pa/index.php/cors) and data access (ftp://168.77.212.59/CORS).
30. Portugal ReNEP: Description (https://renep.dgterritorio.gov.pt/) and data access (ftp://ftp.dgterritorio.pt/ReNEP/).
31. SOPAC: Description (http://sopac-csrc.ucsd.edu/index.php), and data access (http://garner.ucsd.edu/pub/rinex/).
32. SONEL GNSS Stations at Tide Gauges: Description (https://www.sonel.org/-GPS-.html) and data access (ftp://ftp.sonel.org/gps/data).
33. Spain Instituto Geográfico Nacional: Data description (https://www.ign.es/web/gds-gnss-estaciones-permanentes) and data access (https://datos-geodesia.ign.es/ERGNSS/).
34. Sweden SWEPOS: Description (https://www.lantmateriet.se/en/geodata/gps-geodesi-och-swepos/swepos/) and data access (ftp://swepos-open.lantmateriet.se/) (account needed).

9. Summary and Outlook

In this paper, we describe how GNSS data, and in particular various aspects of the position time-series, can be used to gain insight into the structure and properties of the lithosphere and the forces that act on it. By removing known loading signals and/or filtering the time-series, the precision of GNSS time-series and their derived products has increased in recent years. These improvements in precision have allowed for new discoveries such as mantle plume related surface deformation (Kreemer et al., 2020) and aseismic slip preceding great subduction zone earthquakes (Bletery & Nocquet, 2023; Mavrommatis et al., 2014). With increased precision, one ultimate research goal is to associate GNSS-constrained vertical land motions with predicted rates due to dynamic topography; currently, such comparisons are only made qualitatively (Faccenna et al., 2014; Hammond, Blewitt, Kreemer, & Nerem, 2021; Husson et al., 2018; Sternai et al., 2019; Q. Zhao et al., 2023). Another overarching research goal is to leverage precision GNSS data and data products to better understand subsurface processes and structures, such as for magmatic systems, through either inverse modeling (e.g., Daud et al., 2023; Reuber et al., 2018) or forward modeling (e.g., Anderson & Poland, 2016).

15252027, 2024, 7, Downloaded from https://agupubs.onlinelibrary.wiley.com/doi/10.1029/2024GC011567, Wiley Online Library on [16/07/2024]. See the Terms and Conditions (https://onlinelibrary.wiley.com/terms-and-conditions) on Wiley Online Library for rules of use; OA articles are governed by the applicable Creative Commons License

With strain rates in many plate boundaries fairly well constrained, some recent efforts have focused on modeling the strain rates in intraplate areas, notably Europe and North America (Kreemer et al., 2018, 2020; Masson et al., 2019; Piña-Valdés et al., 2022). The proliferation of GNSS stations (and increased access to their data) has helped in these investigations. However, quantifying intraplate deformation is challenging since strain rates are a spatial derivative; thus, any outlier velocities within a dense network can easily be mapped into a local strain rate anomaly. When successful, intraplate strain rate patterns can reveal and constrain, in conjunction with the measured vertical land motions, GIA deformation (e.g., Keiding et al., 2015; Kreemer et al., 2018), the effects of a buoyant mantle plume (Kreemer et al., 2020), or a large-scale sill intrusion (Silverii et al., 2023).

For some data applications, such as interseismic velocities, vertical land motions, and coseismic offsets, GNSS estimates can be augmented with those from other techniques, most notably Interferometric Synthetic Aperture Radar (InSAR). InSAR can provide a more spatially dense estimation but is limited by temporal resolution (currently every week or so), only providing displacements or velocities in the direction of the line-of-sight of the satellite, which is at a high angle from the Earth's surface, and InSAR observations are nearly insensitive to north-south oriented displacements or velocities because of the orbital geometry. Because of these limitations, the most comprehensive results are obtained when combining InSAR and GNSS data in some optimal fashion (e.g., M. Chen et al., 2024; Franklin & Huang, 2022; Maubant et al., 2022; Ou et al., 2022; Watson et al., 2024; W. Wu et al., 2024).

Conflict of Interest

The authors declare no conflicts of interest relevant to this study.

Data Availability Statement

No new data or analyses were used in the development of this review paper. Section 8 of this manuscript, called Resources, provides direct links to numerous open access GNSS data and derived products.

Acknowledgments
Parts of this manuscript are based on services provided by the GAGE Facility, operated by the EarthScope Consortium, with support from the National Science Foundation, the National Aeronautics and Space Administration, and the U.S. Geological Survey under NSF Cooperative Agreement EAR-1724794. We thank Associate Editor John Naliboff, Jeff Freymueller, and an anonymous reviewer for helpful comments that helped improve the manuscript.

References

Abidin, H. Z., Andreas, H., Djaja, R., Darmawan, D., & Gamal, M. (2008). Land subsidence characteristics of Jakarta between 1997 and 2005, as estimated using GPS surveys. *GPS Solutions*, *12*(1), 23–32. https://doi.org/10.1007/s10291-007-0061-0

Agnieszka, W., & Dawid, K. (2022). Modeling seasonal oscillations in GNSS time series with complementary ensemble empirical mode decomposition. *GPS Solutions*, *26*(4), 101. https://doi.org/10.1007/s10291-022-01288-2

Ait-Lakbir, H., Santamaría-Gómez, A., & Perosanz, F. (2023). Impact of the GPS orbital dynamics on spurious interannual Earth deformation. *Geophysical Journal International*, *235*(1), 796–802. https://doi.org/10.1093/gji/ggad268

Altamimi, Z., Rebischung, P., Collilieux, X., Métivier, L., & Chanard, K. (2023). ITRF2020: An augmented reference frame refining the modeling of nonlinear station motions. *Journal of Geodesy*, *97*(5), 47. https://doi.org/10.1007/s00190-023-01738-w

Altamimi, Z., Sillard, P., & Boucher, C. (2006). CATREF software combination and analysis of terrestrial reference frames. Retrieved from https://www5.obs-mip.fr/wp-content-omp/uploads/sites/28/2017/11/CATREF-1.pdf

Amiri-Simkooei, A. R., Tiberius, C. C. J. M., & Teunissen, P. J. G. (2007). Assessment of noise in GPS coordinate time series: Methodology and results. *Journal of Geophysical Research*, *112*(B7), B07413. https://doi.org/10.1029/2006JB004913

Anderson, K. R., & Poland, M. P. (2016). Bayesian estimation of magma supply, storage, and eruption rates using a multiphysical volcano model: Kīlauea Volcano, 2000–2012. *Earth and Planetary Science Letters*, *447*, 161–171. https://doi.org/10.1016/j.epsl.2016.04.029

Argus, D. F., Fu, Y., & Landerer, F. W. (2014). Seasonal variation in total water storage in California inferred from GPS observations of vertical land motion. *Geophysical Research Letters*, *41*(6), 1971–1980. https://doi.org/10.1002/2014GL059570

Argus, D. F., & Gordon, R. G. (1990). Pacific–North American plate motion from very long baseline interferometry compared with motion inferred from magnetic anomalies, transform faults, and earthquake slip vectors. *Journal of Geophysical Research*, *95*(B11), 17315–17324. https://doi.org/10.1029/JB095iB11p17315

Argus, D. F., Gordon, R. G., Heflin, M. B., Ma, C., Eanes, R. J., Willis, P., et al. (2010). The angular velocities of the plates and the velocity of Earth's centre from space geodesy. *Geophysical Journal International*, *180*(3), 913–960. https://doi.org/10.1111/j.1365-246X.2009.04463.x

Argus, D. F., Landerer, F. W., Wiese, D. N., Martens, H. R., Fu, Y., Famiglietti, J. S., et al. (2017). Sustained water loss in California's mountain ranges during severe drought from 2012 to 2015 inferred from GPS. *Journal of Geophysical Research: Solid Earth*, *122*(12), 10559–10585. https://doi.org/10.1002/2017JB014424

Argus, D. F., Peltier, W. R., Blewitt, G., & Kreemer, C. (2021). The viscosity of the top third of the lower mantle estimated using GPS, GRACE, and relative sea level measurements of glacial isostatic adjustment. *Journal of Geophysical Research: Solid Earth*, *126*(5), e2020JB021537. https://doi.org/10.1029/2020JB021537

Argus, D. F., Peltier, W. R., Drummond, R., & Moore, A. W. (2014). The Antarctica component of postglacial rebound model ICE-6G_C (VM5a) based on GPS positioning, exposure age dating of ice thicknesses, and relative sea level histories. *Geophysical Journal International*, *198*(1), 537–563. https://doi.org/10.1093/gji/ggu140

Árnadóttir, T., Jiang, W., Feigl, K. L., Geirsson, H., & Sturkell, E. (2006). Kinematic models of plate boundary deformation in southwest Iceland derived from GPS observations. *Journal of Geophysical Research*, *111*(B7), B07402. https://doi.org/10.1029/2005JB003907

Arnoso, J., Bos, M. S., Benavent, M., Penna, N. T., & Sainz-Maza, S. (2023). Anelastic response of the Earth's crust underneath the Canary Islands revealed from ocean tide loading observations. *Geophysical Journal International*, *235*(1), 273–286. https://doi.org/10.1093/gji/ggad205

Banerjee, P., Pollitz, F., Nagarajan, B., & Bürgmann, R. (2007). Coseismic slip distributions of the 26 December 2004 Sumatra–Andaman and 28 March 2005 Nias earthquakes from GPS static offsets. *Bulletin of the Seismological Society of America*, *97*(1A), S86–S102. https://doi.org/10.1785/0120050609

Banerjee, P., Pollitz, F. F., & Bürgmann, R. (2005). The size and duration of the Sumatra-Andaman earthquake from far-field static offsets. *Science*, *308*(5729), 1769–1772. https://doi.org/10.1126/science.1113746

Beavan, J., & Haines, J. (2001). Contemporary horizontal velocity and strain rate fields of the Pacific-Australian plate boundary zone through New Zealand. *Journal of Geophysical Research*, *106*(B1), 741–770. https://doi.org/10.1029/2000JB900302

Becker, T. W. (2006). On the effect of temperature and strain-rate dependent viscosity on global mantle flow, net rotation, and plate-driving forces. *Geophysical Journal International*, *167*(2), 943–957. https://doi.org/10.1111/j.1365-246x.2006.03172.x

Becker, T. W., & O'Connell, R. J. (2001). Predicting plate velocities with mantle circulation models. *Geochemistry, Geophysics, Geosystems*, *2*(12), 1026. https://doi.org/10.1029/2001gc000171

Bennett, R. A. (2008). Instantaneous deformation from continuous GPS: Contributions from quasi-periodic loads. *Geophysical Journal International*, *174*(3), 1052–1064. https://doi.org/10.1111/j.1365-246X.2008.03846.x

Biessy, G., Moreau, F., Dauteuil, O., & Bour, O. (2011). Surface deformation of an intraplate area from GPS time series. *Journal of Geodynamics*, *52*(1), 24–33. https://doi.org/10.1016/j.jog.2010.11.005

Bird, P. (1998). Testing hypotheses on plate-driving mechanisms with global lithosphere models including topography, thermal structure, and faults. *Journal of Geophysical Research*, *103*(B5), 10115–10129. https://doi.org/10.1029/98jb00198

Bird, P., Liu, Z., & Rucker, W. K. (2008). Stresses that drive the plates from below: Definitions, computational path, model optimization, and error analysis. *Journal of Geophysical Research*, *113*(B11), B11406. https://doi.org/10.1029/2007jb005460

Bird, P., & Piper, K. (1980). Plane-stress finite-element models of tectonic flow in southern California. *Physics of the Earth and Planetary Interiors*, *21*(2–3), 158–175. https://doi.org/10.1016/0031-9201(80)90067-9

Bletery, Q., & Nocquet, J.-M. (2023). The precursory phase of large earthquakes. *Science*, *381*(6655), 297–301. https://doi.org/10.1126/science.adg2565

Blewitt, G. (1989). Carrier phase ambiguity resolution for the Global Positioning System applied to geodetic baselines up to 2000 km. *Journal of Geophysical Research*, *94*(B8), 10187–10203. https://doi.org/10.1029/JB094iB08p10187

Blewitt, G., Hammond, W. C., & Kreemer, C. (2018). Harnessing the GPS data explosion for interdisciplinary science. *Eos*, *99*, 736. https://doi.org/10.1029/2018EO104623

Blewitt, G., Kreemer, C., Hammond, W. C., & Gazeaux, J. (2016). MIDAS robust trend estimator for accurate GPS station velocities without step detection. *Journal of Geophysical Research: Solid Earth*, *121*(3), 2054–2068. https://doi.org/10.1002/2015JB012552

Blewitt, G., Kreemer, C., Hammond, W. C., & Goldfarb, J. M. (2013). Terrestrial reference frame NA12 for crustal deformation studies in North America. *Journal of Geodynamics*, *72*, 11–24. https://doi.org/10.1016/j.jog.2013.08.004

Blewitt, G., & Lavallée, D. (2002). Effect of annual signals on geodetic velocity. *Journal of Geophysical Research*, *107*(B7), B72145. https://doi.org/10.1029/2001JB000570

Bock, Y., & Melgar, D. (2016). Physical applications of GPS geodesy: A review. *Reports on Progress in Physics*, *79*(10), 106801. https://doi.org/10.1088/0034-4885/79/10/106801

Bock, Y., Moore, A. W., Argus, D. F., Fang, P., Jiang, S., Kedar, S., et al. (2021). Extended solid Earth science ESDR system (ES3): Algorithm theoretical basis document: Chapter 4.2.

Bogusz, J., Gruszczynski, M., Figurski, M., & Klos, A. (2015). Spatio-temporal filtering for determination of common mode error in regional GNSS networks. *Open Geosciences*, *7*(1), 140–148. https://doi.org/10.1515/geo-2015-0021

Bos, A. G., Usai, S., & Spakman, W. (2004). A joint analysis of GPS motions and InSAR to infer the coseismic surface deformation of the Izmit, Turkey earthquake. *Geophysical Journal International*, *158*(3), 849–863. https://doi.org/10.1111/j.1365-246X.2004.02359.x

Bos, M. S., Fernandes, R. M. S., Williams, S. D. P., & Bastos, L. (2013). Fast error analysis of continuous GNSS observations with missing data. *Journal of Geodynamics*, *87*(4), 351–360. https://doi.org/10.1007/s00190-012-0605-0

Bos, M. S., Penna, N. T., Baker, T. F., & Clarke, P. J. (2015). Ocean tide loading displacements in western Europe: 2. GPS-observed anelastic dispersion in the asthenosphere. *Journal of Geophysical Research: Solid Earth*, *120*(9), 6540–6557. https://doi.org/10.1002/2015JB011884

Bürgmann, R., & Dresen, G. (2008). Rheology of the lower crust and upper mantle: Evidence from rock mechanics, geodesy, and field observations. *Annual Review of Earth and Planetary Sciences*, *36*(1), 531–567. https://doi.org/10.1146/annurev.earth.36.031207.124326

Calais, E., Ebinger, C., Hartnady, C., & Nocquet, J. M. (2006). Kinematics of the East African Rift from GPS and earthquake slip vector data. *Geological Society, London, Special Publications*, *259*(1), 9–22. https://doi.org/10.1144/GSL.SP.2006.259.01.03

Caporali, A., Martin, S., & Massironi, M. (2003). Average strain rate in the Italian crust inferred from a permanent GPS network—II. Strain rate versus seismicity and structural geology. *Geophysical Journal International*, *155*(1), 254–268. https://doi.org/10.1046/j.1365-246X.2003.02035.x

Cardozo, N., & Allmendinger, R. W. (2009). SSPX: A program to compute strain from displacement/velocity data. *Computers & Geosciences*, *35*(6), 1343–1357. https://doi.org/10.1016/j.cageo.2008.05.008

Chanard, K., Avouac, J. P., Ramillien, G., & Genrich, J. (2014). Modeling deformation induced by seasonal variations of continental water in the Himalaya region: Sensitivity to Earth elastic structure. *Journal of Geophysical Research: Solid Earth*, *119*(6), 5097–5113. https://doi.org/10.1002/2013JB010451

Chanard, K., Fleitout, L., Calais, E., Barbot, S., & Avouac, J.-P. (2018). Constraints on transient viscoelastic rheology of the asthenosphere from seasonal deformation. *Geophysical Research Letters*, *45*(5), 2328–2338. https://doi.org/10.1002/2017GL076451

Chanard, K., Fleitout, L., Calais, E., Rebischung, P., & Avouac, J.-P. (2018). Toward a global horizontal and vertical elastic load deformation model derived from GRACE and GNSS station position time series. *Journal of Geophysical Research: Solid Earth*, *123*(4), 3225–3237. https://doi.org/10.1002/2017JB015245

Chanard, K., Métois, M., Rebischung, P., & Avouac, J.-P. (2020). A warning against over-interpretation of seasonal signals measured by the Global Navigation Satellite System. *Nature Communications*, *11*(1), 1375. https://doi.org/10.1038/s41467-020-15100-7

Chase, C. G. (1972). The N plate problem of plate tectonics. *Geophysical Journal International*, *29*(2), 117–122. https://doi.org/10.1111/j.1365-246X.1972.tb02202.x

Chase, C. G. (1978). Plate kinematics: The Americas, East Africa, and the rest of the world. *Earth and Planetary Science Letters*, *37*(3), 355–368. https://doi.org/10.1016/0012-821X(78)90051-1

Cheloni, D., D'Agostino, N., D'Anastasio, E., Avallone, A., Mantenuto, S., Giuliani, R., et al. (2010). Coseismic and initial post-seismic slip of the 2009 Mw 6.3 L'Aquila earthquake, Italy, from GPS measurements. *Geophysical Journal International*, *181*(3), 1539–1546. https://doi.org/10.1111/j.1365-246x.2010.04584.x

15252027, 2024, 7, Downloaded from https://agupubs.onlinelibrary.wiley.com/doi/10.1029/2024GC011567, Wiley Online Library on [16/07/2024]. See the Terms and Conditions (https://onlinelibrary.wiley.com/terms-and-conditions) on Wiley Online Library for rules of use; OA articles are governed by the applicable Creative Commons License

Chen, M., Xu, G., Zhang, T., Xie, X., & Chen, Z. (2024). A novel method for inverting coseismic 3D surface deformation using InSAR considering the weight influence of the spatial distribution of GNSS points. *Advances in Space Research*, *73*(1), 585–596. https://doi.org/10.1016/j.asr.2023.11.013

Chen, Q., van Dam, T., Sneeuw, N., Collilieux, X., Weigelt, M., & Rebischung, P. (2013). Singular spectrum analysis for modeling seasonal signals from GPS time series. *Journal of Geodynamics*, *72*, 25–35. https://doi.org/10.1016/j.jog.2013.05.005

Chéry, J. (2008). Geodetic strain across the San Andreas fault reflects elastic plate thickness variations (rather than fault slip rate). *Earth and Planetary Science Letters*, *269*(3), 352–365. https://doi.org/10.1016/j.epsl.2008.01.046

Chéry, J., Mohammadi, B., Peyret, M., & Joulain, C. (2011). Plate rigidity inversion in southern California using interseismic GPS velocity field. *Geophysical Journal International*, *187*(2), 783–796. https://doi.org/10.1111/j.1365-246X.2011.05192.x

Ching, K.-E., Rau, R.-J., & Zeng, Y. (2007). Coseismic source model of the 2003 Mw 6.8 Chengkung earthquake, Taiwan, determined from GPS measurements. *Journal of Geophysical Research*, *112*(B6), B06422. https://doi.org/10.1029/2006JB004439

Chlieh, M., De Chabalier, J. B., Ruegg, J. C., Armijo, R., Dmowska, R., Campos, J., & Feigl, K. L. (2004). Crustal deformation and fault slip during the seismic cycle in the North Chile subduction zone, from GPS and InSAR observations. *Geophysical Journal International*, *158*(2), 695–711. https://doi.org/10.1111/j.1365-246X.2004.02326.x

Combrinck, L., & Schmidt, M. (1998). Physical site specifications: Geodetic site monumentation. In *Proceedings of the IGS network workshop* (pp. 91–107).

Conrad, C. P., & Lithgow-Bertelloni, C. (2002). How mantle slabs drive plate tectonics. *Science*, *298*(5591), 207–209. https://doi.org/10.1126/science.1074161

Crocetti, L., Schartner, M., & Soja, B. (2021). Discontinuity detection in GNSS station coordinate time series using machine learning. *Remote Sensing*, *13*(19), 3906. https://doi.org/10.3390/rs13193906

Dach, R., Lutz, S., Walser, P., & Fridez, P. (Eds.) (2015). *Bernese GNSS software version 5.2. User manual*. Astronomical Institute, University of Bern, Bern Open Publishing. https://doi.org/10.7892/boris.72297

D'Agostino, N., Métois, M., Koci, R., Duni, L., Kuka, N., Ganas, A., et al. (2020). Active crustal deformation and rotations in the southwestern Balkans from continuous GPS measurements. *Earth and Planetary Science Letters*, *539*, 116246. https://doi.org/10.1016/j.epsl.2020.116246

D'Agostino, N., Silverii, F., Amoroso, O., Convertito, V., Fiorillo, F., Ventafridda, G., & Zollo, A. (2018). Crustal deformation and seismicity modulated by groundwater recharge of karst aquifers. *Geophysical Research Letters*, *45*(22), 12253–12262. https://doi.org/10.1029/2018GL079794

Daud, N., Stamps, D. S., Battaglia, M., Huang, M. H., Saria, E., & Ji, K. H. (2023). Elucidating the magma plumbing system of Ol Doinyo Lengai (Natron Rift, Tanzania) Using satellite geodesy and numerical modeling. *Journal of Volcanology and Geothermal Research*, *438*, 107821. https://doi.org/10.1016/j.jvolgeores.2023.107821

Davis, J. L., Wernicke, B. P., & Tamisiea, M. E. (2012). On seasonal signals in geodetic time series. *Journal of Geophysical Research*, *117*(B1), B01403. https://doi.org/10.1029/2011JB008690

Decriem, J., & Árnadóttir, T. (2012). Transient crustal deformation in the South Iceland seismic zone observed by GPS and InSAR during 2000–2008. *Tectonophysics*, *581*, 6–18. https://doi.org/10.1016/j.tecto.2011.09.028

DeMets, C., Gordon, R. G., Argus, D. F., & Stein, S. (1990). Current plate motions. *Geophysical Journal International*, *101*(2), 425–478. https://doi.org/10.1111/j.1365-246X.1990.tb06579.x

DeMets, C., Jansma, P. E., Mattioli, G. S., Dixon, T. H., Farina, F., Bilham, R., et al. (2000). GPS geodetic constraints on Caribbean-North America plate motion. *Geophysical Research Letters*, *27*(3), 437–440. https://doi.org/10.1029/1999GL005436

Devoti, R., D'Agostino, N., Serpelloni, E., Pietrantonio, G., Riguzzi, F., Avallone, A., et al. (2017). A combined velocity field of the Mediterranean region. *Annals of Geophysics*, *60*(2), 0215. https://doi.org/10.4401/ag-7059

Diao, F., Xiong, X., Wang, R., Zheng, Y., & Hsu, H. (2011). Slip model of the 2008 Mw 7.9 Wenchuan (China) earthquake derived from co-seismic GPS data. *Earth Planets and Space*, *62*(11), 869–874. https://doi.org/10.5047/eps.2009.05.003

Dong, D., Fang, P., Bock, Y., Cheng, M. K., & Miyazaki, S. (2002). Anatomy of apparent seasonal variations from GPS-derived site position time series. *Journal of Geophysical Research*, *107*(B4), ETG9-1. https://doi.org/10.1029/2001JB000573

Dong, D., Fang, P., Bock, Y., Webb, F., Prawirodirdjo, L., Kedar, S., & Jamason, P. (2006). Spatiotemporal filtering using principal component analysis and Karhunen-Loeve expansion approaches for regional GPS network analysis. *Journal of Geophysical Research*, *111*(B3), B03405. https://doi.org/10.1029/2005JB003806

Dong, D. N., & Bock, Y. (1989). Global positioning system network analysis with phase ambiguity resolution applied to crustal deformation studies in California. *Journal of Geophysical Research*, *94*(B4), 3949–3966. https://doi.org/10.1029/JB094iB04p03949

Donnellan, A., & Lyzenga, G. A. (1998). GPS observations of fault afterslip and upper crustal deformation following the Northridge earthquake. *Journal of Geophysical Research*, *103*(B9), 21285–21297. https://doi.org/10.1029/98JB01487

Drouin, V., Heki, K., Sigmundsson, F., Hreinsdóttir, S., & Ófeigsson, B. G. (2016). Constraints on seasonal load variations and regional rigidity from continuous GPS measurements in Iceland, 1997–2014. *Geophysical Journal International*, *205*(3), 1843–1858. https://doi.org/10.1093/gji/ggw122

El-Fiky, G. S., & Kato, T. (1998). Continuous distribution of the horizontal strain in the Tohoku district, Japan, predicted by least-squares collocation. *Journal of Geodynamics*, *27*(2), 213–236. https://doi.org/10.1016/S0264-3707(98)00006-4

Elliott, J., & Freymueller, J. T. (2020). A block model of present-day kinematics of Alaska and western Canada. *Journal of Geophysical Research: Solid Earth*, *125*(7), e2019JB018378. https://doi.org/10.1130/10.1029/2019JB018378

Elliott, J. L., Larsen, C. F., Freymueller, J. T., & Motyka, R. J. (2010). Tectonic block motion and glacial isostatic adjustment in southeast Alaska and adjacent Canada constrained by GPS measurements. *Journal of Geophysical Research*, *115*(B9), B09407. https://doi.org/10.1029/2009JB007139

England, P., Houseman, G., & Nocquet, J.-M. (2016). Constraints from GPS measurements on the dynamics of deformation in Anatolia and the Aegean. *Journal of Geophysical Research: Solid Earth*, *121*(12), 8888–8916. https://doi.org/10.1002/2016JB013382

England, P., & McKenzie, D. P. (1982). A thin viscous sheet model for continental deformation. *Geophysical Journal of the Royal Astronomical Society*, *70*(2), 321–395. https://doi.org/10.1111/j.1365-246X.1982.tb04969.x

England, P., & Molnar, P. (1997). Active deformation of Asia: From kinematics to dynamics. *Science*, *278*(5338), 647–650. https://doi.org/10.1126/science.278.5338.647

Ergintav, S., McClusky, S., Hearn, E., Reilinger, R., Cakmak, R., Herring, T., et al. (2009). Seven years of postseismic deformation following the 1999, M = 7.4 and M = 7.2, Izmit-Düzce, Turkey earthquake sequence. *Journal of Geophysical Research*, *114*(B7), B07403. https://doi.org/10.1029/2008JB006021

Faccenna, C., Becker, T. W., Miller, M. S., Serpelloni, E., & Willett, S. D. (2014). Isostasy, dynamic topography, and the elevation of the Apennines of Italy. *Earth and Planetary Science Letters*, *407*, 163–174. https://doi.org/10.1016/j.epsl.2014.09.027

15252027, 2024, 7, Downloaded from https://agupubs.onlinelibrary.wiley.com/doi/10.1029/2024GC011567, Wiley Online Library on [16/07/2024]. See the Terms and Conditions (https://onlinelibrary.wiley.com/terms-and-conditions) on Wiley Online Library for rules of use; OA articles are governed by the applicable Creative Commons License

Fang, M., Dong, D., & Hager, B. H. (2014). Displacements due to surface temperature variation on a uniform elastic sphere with its centre of mass stationary. *Geophysical Journal International*, *196*(1), 194–203. https://doi.org/10.1093/gji/ggt335

Farrell, W. E. (1972). Deformation of the Earth by surface loads. *Reviews of Geophysics*, *10*(3), 761–797. https://doi.org/10.1029/RG010i003p00761

Fernandes, R. M. S., Miranda, J. M., Delvaux, D., Stamps, D. S., & Saria, E. (2013). Re-evaluation of the kinematics of Victoria Block using continuous GNSS data. *Geophysical Journal International*, *193*(1), 1–10. https://doi.org/10.1093/gji/ggs071

Finzel, E. S., Flesch, L. M., Ridgway, K. D., Holt, W. E., & Ghosh, A. (2015). Surface motions and intraplate continental deformation in Alaska driven by mantle flow. *Geophysical Research Letters*, *42*(11), 4350–4358. https://doi.org/10.1002/2015GL063987

Flesch, L. M., Haines, J. A., & Holt, W. E. (2001). Dynamics of the India-Eurasia collision zone. *Journal of Geophysical Research*, *106*(B8), 16435–16460. https://doi.org/10.1029/2001jb000208

Flesch, L. M., Holt, W. E., Haines, A. J., & Shen-Tu, B. (2000). Dynamics of the Pacific-North American plate boundary in the western United States. *Science*, *287*(5454), 834–836. https://doi.org/10.1126/science.287.5454.834

Flesch, L. M., Holt, W. E., Haines, A. J., Wen, L., & Shen-Tu, B. (2007). The dynamics of western North America: Stress magnitudes and the relative role of gravitational potential energy, plate interaction at the boundary and basal tractions. *Geophysical Journal International*, *169*(3), 866–896. https://doi.org/10.1111/j.1365-246X.2007.03274.x

Flesch, L. M., & Kreemer, C. (2010). Gravitational potential energy and regional stress and strain rate fields for continental plateaus: Examples from the central Andes and Colorado Plateau. *Tectonophysics*, *482*(1–4), 182–192. https://doi.org/10.1016/j.tecto.2009.07.014

Franklin, K. R., & Huang, M. H. (2022). Revealing crustal deformation and strain rate in Taiwan using InSAR and GNSS. *Geophysical Research Letters*, *49*(21), e2022GL101306. https://doi.org/10.1029/2022GL101306

Freed, A. M., & Bürgmann, R. (2004). Evidence of power-law flow in the Mojave desert mantle. *Nature*, *430*(6999), 548–551. https://doi.org/10.1038/nature02784

Freed, A. M., Bürgmann, R., Calais, E., Freymueller, J., & Hreinsdóttir, S. (2006). Implications of deformation following the 2002 Denali, Alaska, earthquake for postseismic relaxation processes and lithospheric rheology. *Journal of Geophysical Research*, *111*(B1), B01401. https://doi.org/10.1029/2005JB003894

Freymueller, J., King, N. E., & Segall, P. (1994). The co-seismic slip distribution of the Landers earthquake. *Bulletin of the Seismological Society of America*, *84*(3), 646–659. https://doi.org/10.1785/BSSA0840030646

Fu, G., & Sun, W. (2006). Global co-seismic displacements caused by the 2004 Sumatra-Andaman earthquake (Mw 9.1). *Earth Planets and Space*, *58*(2), 149–152. https://doi.org/10.1186/BF03353371

Furst, S., Peyret, M., Chéry, J., & Mohammadi, B. (2018). Lithosphere rigidity by adjoint-based inversion of interseismic GPS data, application to the Western United States. *Tectonophysics*, *746*, 364–383. https://doi.org/10.1016/j.tecto.2017.03.015

Gazeaux, J., Williams, S., King, M., Bos, M., Dach, R., Deo, M., et al. (2013). Detecting offsets in GPS time series: First results from the detection of offsets in GPS experiment. *Journal of Geophysical Research: Solid Earth*, *118*(5), 2397–2407. https://doi.org/10.1002/jgrb.50152

Ge, W.-P., Shen, Z.-K., Molnar, P., Wang, M., Zhang, P.-Z., & Yuan, D.-Y. (2022). GPS determined asymmetric deformation across central Altyn Tagh fault reveals rheological structure of northern Tibet. *Journal of Geophysical Research: Solid Earth*, *127*(9), e2022JB024216. https://doi.org/10.1029/2022JB024216

Ghosh, A., Becker, T., & Humphreys, E. (2013). Dynamics of the North American continent. *Geophysical Journal International*, *194*(2), 651–669. https://doi.org/10.1093/gji/ggt151

Ghosh, A., Holt, W., & Wen, L. (2013). Predicting the lithospheric stress field and plate motions by joint modeling of lithosphere and mantle dynamics. *Journal of Geophysical Research: Solid Earth*, *118*(1), 346–368. https://doi.org/10.1029/2012jb009516

Ghosh, A., & Holt, W. E. (2012). Plate motions and stresses from global dynamic models. *Science*, *335*(6070), 838–843. https://doi.org/10.1126/science.1214209

Ghosh, A., Holt, W. E., Flesch, L. M., & Haines, A. J. (2006). Gravitational potential energy of the Tibetan Plateau and the forces driving the Indian plate. *Geology*, *34*(5), 321–324. https://doi.org/10.1130/G22071.1

Gobron, K., Rebischung, P., Van Camp, M., Demoulin, A., & de Viron, O. (2021). Influence of aperiodic non-tidal atmospheric and oceanic loading deformations on the stochastic properties of global GNSS vertical land motion time series. *Journal of Geophysical Research: Solid Earth*, *126*(9), e2021JB022370. https://doi.org/10.1029/2021JB022370

Gordon, R. G. (1991). Plate motions are steady. *EOS, Transactions American Geophysical Union*, *72*(10), 115. https://doi.org/10.1029/EO072i010p00115-01

Goudarzi, M. A., Cocard, M., & Santerre, R. (2015). GeoStrain: An open source software for calculating crustal strain rates. *Computers & Geosciences*, *82*, 1–12. https://doi.org/10.1016/j.cageo.2015.05.007

Griffiths, J., & Ray, J. (2016). Impacts of GNSS position offsets on global frame stability. *Geophysical Journal International*, *204*(1), 480–487. https://doi.org/10.1093/gji/ggv455

Haas, R., Bergstrand, S., & Lehner, W. (2013). Evaluation of GNSS monument stability. In Z. Altamimi & X. Collilieux (Eds.), *Reference frames for applications in Geosciences. International association of geodesy symposia* (Vol. 138, pp. 45–50). Springer. https://doi.org/10.1007/978-3-642-32998-2_8

Hackl, M., Malservisi, R., & Wdowinski, S. (2009). Strain rate patterns from dense GPS networks. *Natural Hazards and Earth System Sciences*, *9*(4), 1177–1187. https://doi.org/10.5194/nhess-9-1177-2009

Haines, A. J., Dimitrova, L. L., Wallace, L. M., & Williams, C. A. (2015). *Enhanced surface imaging of crustal deformation: Obtaining tectonic force fields using GPS data*. Springer. https://doi.org/10.1007/978-3-319-21578-5

Haines, A. J., & Holt, W. E. (1993). A procedure for obtaining the complete horizontal motions within zones of distributed deformation from the inversion of strain rate data. *Journal of Geophysical Research*, *98*(B7), 12057–12082. https://doi.org/10.1029/93JB00892

Hammond, W. C., Blewitt, G., Kreemer, C., Koehler, R. D., & Dee, S. (2021). Geodetic observation of seismic cycles before, during, and after the 2020 Monte Cristo Range, Nevada earthquake. *Seismological Research Letters*, *92*(2A), 647–662. https://doi.org/10.1785/0220200338

Hammond, W. C., Blewitt, G., Kreemer, C., & Nerem, S. (2021). Global vertical land motion for studies of sea level rise. *J. Geophys. Res. Solid Earth*, *126*(7), e2021JB022355. https://doi.org/10.1029/2021JB022355

Hao, M., Li, Y., & Zhuang, W. (2019). Crustal movement and strain distribution in East Asia revealed by GPS observations. *Scientific Reports*, *9*(1), 16797. https://doi.org/10.1038/s41598-019-53306-y

He, X., Hua, X., Yu, K., Xuan, W., Lu, T., Zhang, W., & Chen, X. (2015). Accuracy enhancement of GPS time series using principal component analysis and block spatial filtering. *Advances in Space Research*, *55*(5), 1316–1327. https://doi.org/10.1016/j.asr.2014.12.016

He, X., Montillet, J. P., Fernandes, R., Bos, M., Yu, K., Hua, X., & Jiang, W. (2017). Review of current GPS methodologies for producing accurate time series and their error sources. *Journal of Geodynamics*, *106*, 12–29. https://doi.org/10.1016/j.jog.2017.01.004

15252027, 2024, 7, Downloaded from https://agupubs.onlinelibrary.wiley.com/doi/10.1029/2024GC011567, Wiley Online Library on [16/07/2024]. See the Terms and Conditions (https://onlinelibrary.wiley.com/terms-and-conditions) on Wiley Online Library for rules of use; OA articles are governed by the applicable Creative Commons License

Hearn, E. H. (2003). What can GPS data tell us about the dynamics of post-seismic deformation? *Geophysical Journal International*, *155*(3), 753–777. https://doi.org/10.1111/j.1365-246X.2003.02030.x

Hearn, E. H., & Bürgmann, R. (2005). The effect of elastic layering on inversions of GPS data for coseismic slip and resulting stress changes: Strike-slip earthquakes. *Bulletin of the Seismological Society of America*, *95*(5), 1637–1653. https://doi.org/10.1785/0120040158

Heister, T., Dannberg, J., Gassmöller, R., & Bangerth, W. (2017). High accuracy mantle convection simulation through modern numerical methods—II: Realistic models and problems. *Geophysical Journal International*, *210*(2), 833–851. https://doi.org/10.1093/gji/ggx195

Herring, T. A. (2003). MATLAB Tools for viewing GPS velocities and time series. *GPS Solutions*, *7*(3), 194–199. https://doi.org/10.1007/s10291-003-0068-0

Herring, T. A., King, R. W., Floyd, M. A., & McClusky, S. C. (2018). Introduction to GAMIT/GLOBK—release 10.7. Retrieved from http://geoweb.mit.edu/gg/Intro_GG.pdf

Herring, T. A., Melbourne, T. I., Murray, M. H., Floyd, M. A., Szeliga, W. M., King, R. W., et al. (2016). Plate boundary observatory and related networks: GPS data analysis methods and geodetic products. *Reviews of Geophysics*, *54*(4), 759–808. https://doi.org/10.1002/2016RG000529

Hirth, G., & Kohlstedf, D. (2003). Rheology of the upper mantle and the mantle wedge: A view from the experimentalists. *Geophysical Monograph-American Geophysical Union*, *138*, 83–106. https://doi.org/10.1029/138GM06

Horner-Johnson, B. C., Gordon, R. G., & Argus, D. F. (2007). Plate kinematic evidence for the existence of a distinct plate between the Nubian and Somalian plates along the Southwest Indian Ridge. *Journal of Geophysical Research*, *112*(B5), BO5418. https://doi.org/10.1029/2006JB004519

Houlié, N., & Romanowicz, B. (2011). Asymmetric deformation across the San Francisco Bay area faults from GPS observations in northern California. *Physics of the Earth and Planetary Interiors*, *184*(3–4), 143–153. https://doi.org/10.1016/j.pepi.2010.11.003

Hreinsdóttir, S., Freymueller, J. T., Fletcher, H. J., Larsen, C. F., & Bürgmann, R. (2003). Coseismic slip distribution of the 2002 MW7.9 Denali fault earthquake, Alaska, determined from GPS measurements. *Geophysical Research Letters*, *30*(13), 1670. https://doi.org/10.1029/2003GL017447

Hu, Y., Bürgmann, R., Banerjee, P., Feng, L., Hill, E. M., Ito, T., et al. (2016). Asthenosphere rheology inferred from observations of the 2012 Indian Ocean earthquake. *Nature*, *538*(7625), 368–372. https://doi.org/10.1038/nature19787

Hu, Y., & Freymueller, J. T. (2019). Geodetic observations of time-variable glacial isostatic adjustment in Southeast Alaska and its implications for Earth rheology. *Journal of Geophysical Research: Solid Earth*, *124*(9), 9870–9889. https://doi.org/10.1029/2018JB017028

Huang, M. H., Bürgmann, R., & Freed, A. M. (2014). Probing the lithospheric rheology across the eastern margin of the Tibetan Plateau. *Earth and Planetary Science Letters*, *396*, 88–96. https://doi.org/10.1016/j.epsl.2014.04.003

Huang, W.-J., & Johnson, K. M. (2012). Strain accumulation across strike-slip faults: Investigation of the influence of laterally varying lithospheric properties. *Journal of Geophysical Research*, *117*(B9), B03404. https://doi.org/10.1029/2012JB009424

Hunstad, I., Anzidei, M., Cocco, M., Baldi, P., Galvani, A., & Pesci, A. (1999). Modelling coseismic displacements during the 1997 Umbria-Marche earthquake (central Italy). *Geophysical Journal International*, *139*(2), 283–295. https://doi.org/10.1046/j.1365-246x.1999.00949.x

Husson, L., Bodin, T., Spada, G., Choblet, G., & Kreemer, C. (2018). Bayesian surface reconstruction of geodetic uplift rates: Mapping the global fingerprint of Glacial Isostatic Adjustment. *Journal of Geodynamics*, *122*, 25–40. https://doi.org/10.1016/j.jog.2018.10.002

Ito, T., & Simons, M. (2011). Probing asthenospheric density, temperature, and elastic moduli below the western United States. *Science*, *332*(6032), 947–951. https://doi.org/10.1126/science.1202584

Jiang, W., Li, Z., van Dam, T., & Ding, W. (2013). Comparative analysis of different environmental loading methods and their impacts on the GPS height time series. *Journal of Geodesy*, *87*(7), 687–703. https://doi.org/10.1007/s00190-013-0642-3

Johanson, I. A., Fielding, E. J., Rolandone, F., & Burgmann, R. (2006). Coseismic and postseismic slip of the 2004 Parkfield earthquake from space-geodetic data. *Bulletin of the Seismological Society of America*, *96*(4B), S269–S282. https://doi.org/10.1785/0120050818

Jolivet, R., Bürgmann, R., & Houlié, N. (2009). Geodetic exploration of the elastic properties across and within the northern San Andreas Fault zone. *Earth and Planetary Science Letters*, *288*(1–2), 126–131. https://doi.org/10.1016/j.epsl.2009.09.014

Kahle, H.-G., Müller, M. V., Geiger, A., Danuser, G., Mueller, S., Veis, G., et al. (1995). The strain field in northwestern Greece and the Ionian Islands: Results inferred from GPS measurements. *Tectonophysics*, *249*(1), 41–52. https://doi.org/10.1016/0040-1951(95)00042-L

Kang, K., Wahr, J., Heflin, M., & Desai, S. (2015). Stacking global GPS verticals and horizontals to solve for the fortnightly and monthly body tides: Implications for mantle anelasticity. *Journal of Geophysical Research: Solid Earth*, *120*(3), 1787–1803. https://doi.org/10.1002/2014JB011572

Keiding, M., Kreemer, C., Lindholm, C. D., Gradmann, S., Olesen, O., & Kierulf, H. P. (2015). A comparison of strain rates and seismicity for Fennoscandia: Depth dependency of deformation from glacial isostatic adjustment. *Geophysical Journal International*, *202*(2), 1021–1028. https://doi.org/10.1093/gji/ggv207

Khazraei, S. M., & Amiri-Simkooei, A. R. (2021). Improving offset detection algorithm of GNSS position time-series using spline function theory. *Geophysical Journal International*, *224*(1), 257–270. https://doi.org/10.1093/gji/ggaa453

King, M. A., Bevis, M., Wilson, T., Johns, B., & Blume, F. (2012). Monument-antenna effects on GPS coordinate time series with application to vertical rates in Antarctica. *Journal of Geodesy*, *86*(1), 53–63. https://doi.org/10.1007/s00190-011-0491-x

King, M. A., & Watson, C. S. (2010). Long GPS coordinate time series: Multipath and geometry effects. *Journal of Geophysical Research*, *115*(B4), B04403. https://doi.org/10.1029/2009JB006543

King, M. A., & Williams, S. D. (2009). Apparent stability of GPS monumentation from short-baseline time series. *Journal of Geophysical Research*, *114*(B10), 10403. https://doi.org/10.1029/2009JB006319

Klos, A., Bos, M. S., & Bogusz, J. (2017). Detecting time-varying seasonal signal in GPS position time series with different noise levels. *GPS Solutions*, *22*(1), 21. https://doi.org/10.1007/s10291-017-0686-6

Klos, A., Dobslaw, H., Dill, R., & Bogusz, J. (2021). Identifying the sensitivity of GPS to non-tidal loadings at various time resolutions: Examining vertical displacements from continental Eurasia. *GPS Solutions*, *25*(3), 89. https://doi.org/10.1007/s10291-021-01135-w

Kogan, M. G., & Steblov, G. M. (2008). Current global plate kinematics from GPS (1995–2007) with the plate-consistent reference frame. *Journal of Geophysical Research*, *113*(B4), B04416. https://doi.org/10.1029/2007JB005353

Koulali, A., & Clarke, P. J. (2021). Modelling quasi-periodic signals in geodetic time-series using Gaussian processes. *Geophysical Journal International*, *226*(3), 1705–1714. https://doi.org/10.1093/gji/ggab168

Koulali, A., Ouazar, D., Tahayt, A., King, R. W., Vernant, P., Reilinger, R. E., et al. (2011). New GPS constraints on active deformation along the Africa–Iberia plate boundary. *Earth and Planetary Science Letters*, *308*(1–2), 211–217. https://doi.org/10.1016/j.epsl.2011.05.048

Kreemer, C., & Blewitt, G. (2021). Robust estimation of spatially varying common-mode components in GPS time-series. *Journal of Geodesy*, *95*(1), 13. https://doi.org/10.1007/s00190-020-01466-5

Kreemer, C., Blewitt, G., & Davis, P. M. (2020). Geodetic evidence for a buoyant mantle plume beneath the Eifel volcanic area, NW Europe. *Geophysical Journal International*, *222*(2), 1316–1332. https://doi.org/10.1093/gji/ggaa227

15252027, 2024, 7, Downloaded from https://agupubs.onlinelibrary.wiley.com/doi/10.1029/2024GC011567, Wiley Online Library on [16/07/2024]. See the Terms and Conditions (https://onlinelibrary.wiley.com/terms-and-conditions) on Wiley Online Library for rules of use; OA articles are governed by the applicable Creative Commons License

Kreemer, C., Blewitt, G., Hammond, W. C., & Plag, H.-P. (2006). Global deformation from the great 2004 Sumatra-Andaman Earthquake observed by GPS: Implications for rupture process and global reference frame. *Earth Planets and Space*, *58*(2), 141–148. https://doi.org/10.1186/BF03353370

Kreemer, C., Blewitt, G., & Klein, E. C. (2014). A geodetic plate motion and global strain rate model. *Geochemistry, Geophysics, Geosystems*, *15*(10), 3849–3889. https://doi.org/10.1002/2014GC005407

Kreemer, C., Blewitt, G., & Maerten, F. (2006). Co- and postseismic deformation of the 28 March 2005 Nias Mw 8.7 earthquake from continuous GPS data. *Geophysical Research Letters*, *33*(7), L07307. https://doi.org/10.1029/2005gl025566

Kreemer, C., & Chamot-Rooke, N. (2004). Contemporary kinematics of the southern Aegean and the Mediterranean ridge. *Geophysical Journal International*, *157*(3), 1377–1392. https://doi.org/10.1111/j.1365-246X.2004.02270.x

Kreemer, C., Hammond, W. C., & Blewitt, G. (2018). A robust estimation of the 3-D intraplate deformation of the North American plate from GPS. *Journal of Geophysical Research: Solid Earth*, *123*(5), 4388–4412. https://doi.org/10.1029/2017JB015257

Kreemer, C., & Young, Z. M. (2022). Crustal strain rates in the Western U.S. and their relationship with earthquake rates. *Seismological Research Letters*, *93*(6), 2990–3008. https://doi.org/10.1785/0220220153

Kronbichler, M., Heister, T., & Bangerth, W. (2012). High accuracy mantle convection simulation through modern numerical methods. *Geophysical Journal International*, *191*(1), 12–29. https://doi.org/10.1111/j.1365-246X.2012.05609.x

Lahtinen, S., Jivall, L., Häkli, P., & Nordman, M. (2021). Updated GNSS velocity solution in the Nordic and Baltic countries with a semi-automatic offset detection method. *GPS Solutions*, *26*(1), 9. https://doi.org/10.1007/s10291-021-01194-z

Langbein, J. (2017). Improved efficiency of maximum likelihood analysis of time series with temporally correlated errors. *Journal of Geodesy*, *91*(8), 985–994. https://doi.org/10.1007/s00190-017-1002-5

Langbein, J. (2020). Methods for rapidly estimating velocity precision from GNSS time series in the presence of temporal correlation: A new method and comparison of existing methods. *Journal of Geophysical Research: Solid Earth*, *125*(7), e2019JB019132. https://doi.org/10.1029/2019JB019132

Le Pichon, X. (1968). Sea-floor spreading and continental drift. *Journal of Geophysical Research*, *73*(12), 3661–3697. https://doi.org/10.1029/JB073i012p03661

Le Pichon, X., Kreemer, C., & Chamot-Rooke, N. (2005). Asymmetry in elastic properties and the evolution of large continental strike-slip faults. *Journal of Geophysical Research*, *110*(B3), B03405. https://doi.org/10.1029/2004JB003343

Lindsey, E. O., Wang, Y., Aung, L. T., Chong, J. H., Qiu, Q., Mallick, R., et al. (2023). Active subduction and strain partitioning in western Myanmar revealed by a dense survey GNSS network. *Earth and Planetary Science Letters*, *622*, 118384. https://doi.org/10.1016/j.epsl.2023.118384

Lisowski, M., Prescott, W. H., Savage, J. C., & John-stone, M. J. S. (1990). Geodetic estimate of co-seismic slip during the 1989 Loma Prieta, California, earthquake. *Geophysical Research Letters*, *17*(9), 1437–1440. https://doi.org/10.1146/annurev.earth.25.1.301

Liu, S., & King, S. D. (2022). Dynamics of the North American plate: Large-scale driving mechanism from far-field slabs and the interpretation of shallow negative seismic anomalies. *Geochemistry, Geophysics, Geosystems*, *23*(3), e2021GC009808. https://doi.org/10.1029/2021GC009808

Liu, S., Xu, X., Klinger, Y., Nocquet, J. M., Chen, G., Yu, G., & Jónsson, S. (2019). Lower crustal heterogeneity beneath the northern Tibetan Plateau constrained by GPS measurements following the 2001 Mw7. 8 Kokoxili earthquake. *Journal of Geophysical Research: Solid Earth*, *124*(11), 11992–12022. https://doi.org/10.1029/2019JB017732

Liu-Zeng, J., Zhang, Z., Rollins, C., Gualandi, A., Avouac, J.-P., Shi, H., et al. (2020). Postseismic deformation following the 2015 Mw7.8 Gorkha (Nepal) earthquake: New GPS data, kinematic and dynamic models, and the roles of afterslip and viscoelastic relaxation. *Journal of Geophysical Research: Solid Earth*, *125*(9), e2020JB019852. https://doi.org/10.1029/2020JB019852

Mao, A., Harrison, C. G. A., & Dixon, T. H. (1999). Noise in GPS coordinate time series. *Journal of Geophysical Research*, *104*(B2), 2797–2816. https://doi.org/10.1029/1998JB900033

Marone, C. J., Scholz, C. H., & Bilham, R. (1991). On the mechanics of earthquake afterslip. *Journal of Geophysical Research*, *96*(B5), 8441–8452. https://doi.org/10.1029/91JB00275

Márquez-Azúa, B., & DeMets, C. (2003). Crustal velocity field of Mexico from continuous GPS measurements, 1993 to June 2001: Implications for the neotectonics of Mexico. *Journal of Geophysical Research*, *108*(B9), 2450. https://doi.org/10.1029/2002JB002241

Martens, H. R., Argus, D. F., Norberg, C., Blewitt, G., Herring, T. A., Moore, A. W., et al. (2020). Atmospheric pressure loading in GPS positions: Dependency on GPS processing methods and effect on assessment of seasonal deformation in the contiguous USA and Alaska. *Journal of Geodesy*, *94*(12), 115. https://doi.org/10.1007/s00190-020-01445-w

Martens, H. R., Rivera, L., & Simons, M. (2019). LoadDef: A Python-based Toolkit to model elastic deformation caused by surface mass loading on spherically symmetric bodies. *Earth and Space Science*, *6*(2), 311–323. https://doi.org/10.1029/2018EA000462

Martens, H. R., & Simons, M. (2020). A comparison of predicted and observed ocean tidal loading in Alaska. *Geophysical Journal International*, *223*(1), 454–470. https://doi.org/10.1093/gji/ggaa323

Martens, H. R., Simons, M., Owen, S., & Rivera, L. (2016). Observations of ocean tidal load response in South America from subdaily GPS positions. *Geophysical Journal International*, *205*(3), 1637–1664. https://doi.org/10.1093/gji/ggw087

Masson, C., Mazzotti, S., Vernant, P., & Doerflinger, E. (2019). Extracting small deformation beyond individual station precision from dense Global Navigation Satellite System (GNSS) networks in France and western Europe. *Solid Earth*, *10*(6), 1905–1920. https://doi.org/10.5194/se-10-1905-2019

Materna, K., Maurer, J., & Sandoe, L. (2021). kmaterna/Strain_2D: First release. *Zenodo*. https://doi.org/10.5281/zenodo.5240908

Matviichuk, B., King, M. A., Watson, C. S., & Bos, M. S. (2021). Limitations in one-dimensional (an)Elastic Earth models for explaining GPS-observed M2 ocean tide loading displacements in New Zealand. *Journal of Geophysical Research: Solid Earth*, *126*(6), e2021JB021992. https://doi.org/10.1029/2021jb021992

Maubant, L., Radiguet, M., Pathier, E., Doin, M.-P., Cotte, N., Kazachkina, E., & Kostoglodov, V. (2022). Interseismic coupling along the Mexican subduction zone seen by InSAR and GNSS. *Earth and Planetary Science Letters*, *586*, 117534. https://doi.org/10.1016/j.epsl.2022.117534

Mavrommatis, A. P., Segall, P., & Johnson, K. M. (2014). A decadal-scale deformation transient prior to the 2011 Mw 9.0 Tohoku-oki earthquake. *Geophysical Research Letters*, *41*(13), 4486–4494. https://doi.org/10.1002/2014GL060139

McCaffrey, R. (2009). Time-dependent inversion of three-component continuous GPS for steady and transient sources in northern Cascadia. *Geophysical Research Letters*, *36*(7), L07304. https://doi.org/10.1029/2008GL036784

Meade, B. J., & Hager, B. H. (2005). Block models of crustal motion in southern California constrained by GPS measurements. *Journal of Geophysical Research*, *110*(B3), B03403. https://doi.org/10.1029/2004JB003209

Meade, B. J., & Loveless, J. P. (2009). Block modeling with multiple fault network geometries and a linear elastic coupling estimator in spherical coordinates. *Bulletin of the Seismological Society of America*, *99*(6), 3124–3139. https://doi.org/10.1785/0120090088

15252027, 2024, 7, Downloaded from https://agupubs.onlinelibrary.wiley.com/doi/10.1029/2024GC011567, Wiley Online Library on [16/07/2024]. See the Terms and Conditions (https://onlinelibrary.wiley.com/terms-and-conditions) on Wiley Online Library for rules of use; OA articles are governed by the applicable Creative Commons License

Métois, M., D'Agostino, N., Avallone, A., Chamot-Rooke, N., Rabaute, A., Duni, L., et al. (2015). Insights on continental collisional processes from GPS data: Dynamics of the peri-Adriatic belts. *Journal of Geophysical Research: Solid Earth*, *120*(12), 8701–8719. https://doi.org/10.1002/2015JB012023

Milliner, C., Materna, K., Bürgmann, R., Fu, Y., Moore, A. W., Bekaert, D., et al. (2018). Tracking the weight of Hurricane Harvey's stormwater using GPS data. *Science Advances*, *4*(9), eaau2477. https://doi.org/10.1126/sciadv.aau2477

Minster, J. B., & Jordan, T. H. (1978). Present-day plate motions. *Journal of Geophysical Research*, *83*(B11), 5331–5354. https://doi.org/10.1029/JB083iB11p05331

Moresi, L., Zhong, S., Han, L., Conrad, C., Tan, E., Gurnis, M., et al. (2014). CitcomS v3.3.1 (v3.3.1). *Zenodo*. https://doi.org/10.5281/zenodo.7271920

Murray, K. D., Murray, M. H., & Sheehan, A. F. (2019). Active deformation near the Rio Grande rift and Colorado plateau as inferred from continuous global positioning system measurements. *Journal of Geophysical Research: Solid Earth*, *124*(2), 2166–2183. https://doi.org/10.1029/2018JB016626

Nikolaidis, R. (2002). *Observation of geodetic and seismic deformation with the global positioning system, Ph.D Thesis* (p. 305). University of California.

Njoroge, M., Malservisi, R., Voytenko, D., & Hackl, M. (2017). Is Nubia plate rigid? A geodetic study of the relative motion of different cratonic areas within Africa. In *REFAG 2014: Proceedings of the IAG Commission 1 symposium Kirchberg, Luxembourg, 13–17 October, 2014* (pp. 171–180). Springer International Publishing.

Noda, A., & Matsu'ura, M. (2010). Physics-based GPS data inversion to estimate three-dimensional elastic and inelastic strain fields. *Geophysical Journal International*, *182*(2), 513–530. https://doi.org/10.1111/j.1365-246X.2010.04611.x

Noll, C. E. (2010). The crustal dynamics data information system: A resource to support scientific analysis using space geodesy. *Advances in Space Research*, *45*(12), 1421–1440. https://doi.org/10.1016/j.asr.2010.01.018

Norabuena, E. O., Dixon, T. H., Stein, S., & Harrison, C. G. (1999). Decelerating Nazca-south America and Nazca-Pacific plate motions. *Geophysical Research Letters*, *26*(22), 3405–3408. https://doi.org/10.1029/1999GL005394

Ohta, Y., Hino, R., Inazu, D., Ohzono, M., Ito, Y., Mishina, M., et al. (2012). Geodetic constraints on afterslip characteristics following the March 9, 2011, Sanriku-oki earthquake, Japan. *Geophysical Research Letters*, *39*(16), L16304. https://doi.org/10.1029/2012GL052430

Okada, Y. (1985). Surface deformation due to shear and tensile faults in a half-space. *Bulletin of the Seismological Society of America*, *75*(4), 1135–1154. https://doi.org/10.1785/BSSA0750041135

Okazaki, T., Fukahata, Y., & Nishimura, T. (2021). Consistent estimation of strain-rate fields from GNSS velocity data using basis function expansion with ABIC. *Earth Planets and Space*, *73*(1), 153. https://doi.org/10.1186/s40623-021-01474-5

Ou, Q., Daout, S., Weiss, J. R., Shen, L., Lazecký, M., Wright, T. J., & Parsons, B. E. (2022). Large-scale interseismic strain mapping of the NE Tibetan plateau from Sentinel-1 interferometry. *Journal of Geophysical Research: Solid Earth*, *127*(6), e2022JB024176. https://doi.org/10.1029/2022JB024176

Özarpacı, S., Doğan, U., Ergintav, S., Çakır, Z., Özdemir, A., Floyd, M., & Reilinger, R. (2021). Present GPS velocity field along 1999 Izmit rupture zone: Evidence for continuing afterslip 20 yr after the earthquake. *Geophysical Journal International*, *224*(3), 2016–2027. https://doi.org/10.1093/gji/ggaa560

Ozawa, S., Nishimura, T., Suito, H., Kobayashi, T., Tobita, M., & Imakiire, T. (2011). Coseismic and postseismic slip of the 2011 magnitude-9 Tohoku-Oki earthquake. *Nature*, *475*(7356), 373–376. https://doi.org/10.1038/nature10227

Özeren, M. S., & Holt, W. E. (2010). The dynamics of the eastern Mediterranean and eastern Turkey. *Geophysical Journal International*, *183*(3), 1165–1184. https://doi.org/10.1111/j.1365-246X.2010.04819.x

Pagani, C., Bodin, T., Metois, M., & Lasserre, C. (2021). Bayesian estimation of surface strain rates from Global Navigation Satellite System measurements: Application to the southwestern United States. *Journal of Geophysical Research Solid Earth*, *126*(6), e2021JB021905. https://doi.org/10.1029/2021JB021905

Park, S., Avouac, J.-P., Zhan, Z., & Gualandi, A. (2023). Weak upper-mantle base revealed by postseismic deformation of a deep earthquake. *Nature*, *615*(7952), 455–460. https://doi.org/10.1038/s41586-022-05689-8

Perfettini, H., & Avouac, J. P. (2004). Postseismic relaxation driven by brittle creep: A possible mechanism to reconcile geodetic measurements and the decay rate of aftershocks, application to the Chi-Chi earthquake, Taiwan. *Journal of Geophysical Research*, *109*(B2), B02304. https://doi.org/10.1029/2003JB002488

Pietrantonio, G., & Riguzzi, F. (2004). Three-dimensional strain tensor estimation by GPS observations: Methodological aspects and geophysical applications. *Journal of Geodynamics*, *38*(1), 1–18. https://doi.org/10.1016/j.jog.2004.02.021

Piña-Valdés, J., Socquet, A., Beauval, C., Doin, M.-P., D'Agostino, N., & Shen, Z.-K. (2022). 3D GNSS velocity field Sheds light on the deformation mechanisms in Europe: Effects of the vertical crustal motion on the distribution of seismicity. *Journal of Geophysical Research: Solid Earth*, *127*(6), e2021JB023451. https://doi.org/10.1029/2021JB023451

Pollitz, F. F. (1996). Coseismic deformation from earthquake faulting on a layered spherical Earth. *Geophysical Journal International*, *125*(1), 1–14. https://doi.org/10.1111/j.1365-246X.1996.tb06530.x

Pollitz, F. F. (2015). Postearthquake relaxation evidence for laterally variable viscoelastic structure and water content in the Southern California mantle. *Journal of Geophysical Research: Solid Earth*, *120*(4), 2672–2696. https://doi.org/10.1002/2014JB011603

Pollitz, F. F., Bürgmann, R., & Banerjee, P. (2011). Geodetic slip model of the 2011 M9.0 Tohoku earthquake. *Geophysical Research Letters*, *38*(7), L00G14. https://doi.org/10.1029/2011GL048632

Prawirodirdjo, L., Ben-Zion, Y., & Bock, Y. (2006). Observation and modeling of thermoelastic strain in Southern California Integrated GPS Network daily position time series. *Journal of Geophysical Research*, *111*(B2), B02408. https://doi.org/10.1029/2005JB003716

Prescott, W. H., & Nur, A. (1981). The accommodation of relative motion at depth on the San Andreas Fault System in California. *Journal of Geophysical Research*, *86*(B2), 999–1004. https://doi.org/10.1029/JB086iB02p00999

Rajaonarison, T. A., Stamps, D. S., & Naliboff, J. (2021). Role of lithospheric buoyancy forces in driving deformation in East Africa from 3D geodynamic modeling. *Geophysical Research Letters*, *48*(6), e2020GL090483. https://doi.org/10.1029/2020GL090483

Rajaonarison, T. A., Stamps, D. S., Naliboff, J., Nyblade, A., & Njinju, E. A. (2023). A geodynamic investigation of plume-lithosphere interactions beneath the East African rift. *Journal of Geophysical Research: Solid Earth*, *128*(4), e2022JB025800. https://doi.org/10.1029/2022JB025800

Ramírez-Zelaya, J., Peci, L. M., Fernández-Ros, A., Rosado, B., Pérez-Peña, A., Gárate, J., & Berrocoso, M. (2023). Q–Str2–Models: A software in PyQGIS to obtain stress–strain models from GNSS geodynamic velocities. *Computers & Geosciences*, *172*, 105308. https://doi.org/10.1016/j.cageo.2023.105308

Ray, J., Altamimi, Z., Collilieux, X., & van Dam, T. (2008). Anomalous harmonics in the spectra of GPS position estimates. *GPS Solutions*, *12*(1), 55–64. https://doi.org/10.1007/s10291-007-0067-7

15252027, 2024, 7, Downloaded from https://agupubs.onlinelibrary.wiley.com/doi/10.1029/2024GC011567, Wiley Online Library on [16/07/2024]. See the Terms and Conditions (https://onlinelibrary.wiley.com/terms-and-conditions) on Wiley Online Library for rules of use; OA articles are governed by the applicable Creative Commons License

Reilinger, R. E., Ergintav, S., Bürgmann, R., McClusky, S., Lenk, O., Barka, A., et al. (2000). Coseismic and postseismic fault slip for the 17 August 1999, M = 7.5, Izmit, Turkey earthquake. *Science*, *289*(5484), 1519–1524. https://doi.org/10.1126/science.289.5484.1519

Reilinger, R. E., McClusky, S., Vernant, P., Lawrence, S., Ergintav, S., Cakmak, R., et al. (2006). GPS constraints on continental deformation in the Africa-Arabia-Eurasia continental collision zone and implications for the dynamics of plate interactions. *Journal of Geophysical Research*, *111*(B5), B05411. https://doi.org/10.1029/2005JB004051

Reuber, G. S., Kaus, B. J. P., Popov, A. A., & Baumann, T. S. (2018). Unraveling the physics of the Yellowstone magmatic system using geodynamic Simulations. *Frontiers in Earth Science*, *6*, 117. https://doi.org/10.3389/feart.2018.00117

Robbins, J. W., Smith, D. E., & Ma, C. (1993). Horizontal crustal deformation and large scale plate motions inferred from space geodetic techniques. Contributions of Space Geodesy to Geodynamics. *Crustal Dynamics*, *23*, 21–36. https://doi.org/10.1029/GD023

Romagnoli, C., Zerbini, S., Lago, L., Richter, B., Simon, D., Domenichini, F., et al. (2003). Influence of soil consolidation and thermal expansion effects on height and gravity variations. *Journal of Geodynamics*, *35*(4), 521–539. https://doi.org/10.1016/S0264-3707(03)00012-7

Rui, X., & Stamps, D. S. (2016). Present-day kinematics of the eastern Tibetan Plateau and Sichuan Basin: Implications for lower crustal rheology. *Journal of Geophysical Research: Solid Earth*, *121*(5), 3846–3866. https://doi.org/10.1002/2016JB012839

Rui, X., & Stamps, D. S. (2019). A geodetic strain rate and tectonic velocity model for China. *Geochemistry, Geophysics, Geosystems*, *20*(3), 1280–1297. https://doi.org/10.1029/2018GC007806

Sandwell, D. T., & Wessel, P. (2016). Interpolation of 2-D vector data using constraints from elasticity. *Geophysical Research Letters*, *43*(20), 10703–10709. https://doi.org/10.1002/2016GL070340

Santamaría-Gómez, A., Bouin, M.-N., Collilieux, X., & Wöppelmann, G. (2011). Correlated errors in GPS position time series: Implications for velocity estimates. *Journal of Geophysical Research*, *116*(B1), B01405. https://doi.org/10.1029/2010JB007701

Santamaría-Gómez, A., Gravelle, M., Dangendorf, S., Marcos, M., Spada, G., & Wöppelmann, G. (2017). Uncertainty of the 20th century sea-level rise due to vertical land motion errors. *Earth and Planetary Science Letters*, *473*, 24–32. https://doi.org/10.1016/j.epsl.2017.05.038

Saria, E., Calais, E., Altamimi, Z., Willis, P., & Farah, H. (2013). A new velocity field for Africa from combined GPS and DORIS space geodetic solutions: Contribution to the definition of the African reference frame (AFREF). *Journal of Geophysical Research: Solid Earth*, *118*(4), 1677–1697. https://doi.org/10.1002/jgrb.50137

Saria, E., Calais, E., Stamps, D. S., Delvaux, D., & Hartnady, C. J. H. (2014). Present-day kinematics of the East African Rift. *Journal of Geophysical Research: Solid Earth*, *119*(4), 3584–3600. https://doi.org/10.1002/2013JB010901

Savage, J. C., & Burford, R. O. (1973). Geodetic determination of relative plate motion in central California. *Journal of Geophysical Research*, *78*(5), 832–845. https://doi.org/10.1029/jb078i005p00832

Savage, J. C., & Prescott, W. H. (1978). Asthenosphere readjustment and the earthquake cycle. *Journal of Geophysical Research*, *83*(B7), 3369–3376. https://doi.org/10.1029/JB083iB07p03369

Saxena, A., Dannberg, J., Gassmöller, R., Fraters, M., Heister, T., & Styron, R. (2023). High-resolution mantle flow models reveal importance of plate boundary geometry and slab pull forces on generating tectonic plate motions. *Journal of Geophysical Research: Solid Earth*, *128*(8), e2022JB025877. https://doi.org/10.1029/2022JB025877

Schmalzle, G., Dixon, T., Malservisi, R., & Govers, R. (2006). Strain accumulation across the Carrizo segment of the San Andreas Fault, California: Impact of laterally varying crustal properties. *Journal of Geophysical Research*, *111*(B5), B05403. https://doi.org/10.1029/2005JB003843

Scholz, C. H. (1998). Earthquakes and friction laws. *Nature*, *391*(6662), 37–42. https://doi.org/10.1038/34097

Segall, P. (2010). *Earthquake and volcano deformation*. Princeton University Press. https://doi.org/10.1515/9781400833856

Sella, G. F., Stein, S., Dixon, T. H., Craymer, M., James, T. S., Mazzotti, S., & Dokka, R. K. (2007). Observation of glacial isostatic adjustment in "stable" North America with GPS. *Geophysical Research Letters*, *34*(2), L02306. https://doi.org/10.1029/2006GL027081

Shen, Y., Li, W., Xu, G., & Li, B. (2014). Spatiotemporal filtering of regional GNSS network's position time series with missing data using principle component analysis. *Journal of Geodesy*, *88*(1), 1–12. https://doi.org/10.1007/s00190-013-0663-y

Shen, Z.-K., Jackson, D. D., & Ge, B. X. (1996). Crustal deformation across and beyond the Los Angeles basin from geodetic measurements. *Journal of Geophysical Research*, *101*(B12), 27957–27980. https://doi.org/10.1029/96JB02544

Shen, Z.-K., Jackson, D. D., & Kagan, Y. Y. (2007). Implications of geodetic strain rate for future earthquakes, with a five-year forecast of M5 earthquakes in southern California. *Seismological Research Letters*, *78*(1), 116–120. https://doi.org/10.1785/gssrl.78.1.116

Shen, Z.-K., Wang, M., Zeng, Y., & Wang, F. (2015). Optimal interpolation of spatially discretized geodetic data. *Bulletin of the Seismological Society of America*, *105*(4), 2117–2127. https://doi.org/10.1785/0120140247

Silverii, F., D'Agostino, N., Métois, M., Fiorillo, F., & Ventafridda, G. (2016). Transient deformation of karst aquifers due to seasonal and multiyear groundwater variations observed by GPS in southern Apennines (Italy). *Journal of Geophysical Research: Solid Earth*, *121*(11), 8315–8337. https://doi.org/10.1002/2016JB013361

Silverii, F., Mantiloni, L., Rivalta, E., & Dahm, T. (2023). Lithospheric sill intrusions and present-day ground deformation at Rhenish Massif, central Europe. *Geophysical Research Letters*, *50*(23), e2023GL105824. https://doi.org/10.1029/2023GL105824

Simon, K. M., Riva, R. E. M., Kleinherenbrink, M., & Frederikse, T. (2018). The glacial isostatic adjustment signal at present day in northern Europe and the British Isles estimated from geodetic observations and geophysical models. *Solid Earth*, *9*(3), 777–795. https://doi.org/10.5194/se-9-777-2018

Smith, S. W., & Wyss, M. (1968). Displacement on the san Andreas fault subsequent to the 1966 Parkfield earthquake. *Bulletin of the Seismological Society of America*, *58*(6), 1955–1973. https://doi.org/10.1785/BSSA0580061955

Sobrero, F. S., Bevis, M., Gómez, D. D., & Wang, F. (2020). Logarithmic and exponential transients in GNSS trajectory models as indicators of dominant processes in postseismic deformation. *Journal of Geodesy*, *94*(9), 84. https://doi.org/10.1007/s00190-020-01413-4

Stamps, D. S., Calais, E., Saria, E., Hartnady, C., Nocquet, J. M., Ebinger, C. J., & Fernandes, R. M. (2008). A kinematic model for the East African Rift. *Geophysical Research Letters*, *35*(5), L14315. https://doi.org/10.1029/2007GL032781

Stamps, D. S., Flesch, L. M., Calais, E., & Ghosh, A. (2014). Current kinematics and dynamics of Africa and the East African Rift System. *Journal of Geophysical Research: Solid Earth*, *119*(6), 5161–5186. https://doi.org/10.1002/2013JB010717

Stamps, D. S., Iaffaldano, G., & Calais, E. (2015). Role of mantle flow in Nubia-Somalia plate divergence. *Geophysical Research Letters*, *42*(2), 290–296. https://doi.org/10.1002/2014GL062515

Stamps, D. S., Kreemer, C., Fernandes, R., Rajaonarison, T. A., & Rambolamanana, G. (2021). Redefining east African rift system kinematics. *Geology*, *49*(2), 150–155. https://doi.org/10.1130/G47985.1

Stamps, D. S., Saria, E., & Kreemer, C. (2018). A geodetic strain rate model for the East African Rift System. *Scientific Reports*, *8*(1), 732. https://doi.org/10.1038/s41598-017-19097-w

Sternai, P., Sue, C., Husson, L., Serpelloni, E., Becker, T. W., Willett, S. D., et al. (2019). Present-day uplift of the European Alps: Evaluating mechanisms and models of their relative contributions. *Earth-Science Reviews*, *190*, 589–604. https://doi.org/10.1016/j.earscirev.2019.01.005

15252027, 2024, 7, Downloaded from https://agupubs.onlinelibrary.wiley.com/doi/10.1029/2024GC011567, Wiley Online Library on [16/07/2024]. See the Terms and Conditions (https://onlinelibrary.wiley.com/terms-and-conditions) on Wiley Online Library for rules of use; OA articles are governed by the applicable Creative Commons License

Stevens, V. L., & Avouac, J.-P. (2021). On the relationship between strain rate and seismicity in the India–Asia collision zone: Implications for probabilistic seismic hazard. *Geophysical Journal International*, *226*(1), 220–245. https://doi.org/10.1093/gji/ggab098
Su, X., Yao, L., Wu, W., Meng, G., Su, L., Xiong, R., & Hong, S. (2019). Crustal deformation on the Northeastern margin of the Tibetan plateau from continuous GPS observations. *Remote Sensing*, *11*(1), 34. https://doi.org/10.3390/rs11010034
Sun, W., Okubo, S., & Vaníček, P. (1996). Global displacements caused by point dislocations in a realistic Earth model. *Journal of Geophysical Research*, *101*(B4), 8561–8577. https://doi.org/10.1029/95JB03536
Tape, C., Musé, P., Simons, M., Dong, D., & Webb, F. (2009). Multiscale estimation of GPS velocity fields. *Geophysical Journal International*, *179*(2), 945–971. https://doi.org/10.1111/j.1365-246X.2009.04337.x
Teunissen, P. J. & Montenbruck, O. (Eds.) (2017). *Springer handbook of global navigation satellite systems* (Vol. 10). Springer International Publishing. https://doi.org/10.1007/978-3-319-42928-1
Teza, G., Pesci, A., & Meschis, M. (2023). A MATLAB toolbox for computation of velocity and strain rate field from GNSS coordinate time series. *Annals of Geophysics*, *66*. https://doi.org/10.4401/ag-8933
Tian, Y., & Shen, Z.-K. (2016). Extracting the regional common-mode component of GPS station position time series from dense continuous network. *Journal of Geophysical Research: Solid Earth*, *121*(2), 1080–1096. https://doi.org/10.1002/2015JB012253
Tobita, M. (2016). Combined logarithmic and exponential function model for fitting postseismic GNSS time series after 2011 Tohoku-Oki earthquake. *Earth Planets and Space*, *68*(1), 41. https://doi.org/10.1186/s40623-016-0422-4
Traoré, N., Le Pourhiet, L., Frelat, J., Rolandone, F., & Meyer, B. (2014). Does interseismic strain localization near strike-slip faults result from boundary conditions or rheological structure? *Geophysical Journal International*, *197*(1), 50–62. https://doi.org/10.1093/gji/ggu011
Tregoning, P., Burgette, R., McClusky, S. C., Lejeune, S., Watson, C. S., & McQueen, H. (2013). A decade of horizontal deformation from great earthquakes. *Journal of Geophysical Research: Solid Earth*, *118*(5), 2371–2381. https://doi.org/10.1002/jgrb.50154
Tsai, V. C. (2011). A model for seasonal changes in GPS positions and seismic wave speeds due to thermoelastic and hydrologic variations. *Journal of Geophysical Research*, *116*(B4), B04404. https://doi.org/10.1029/2010JB008156
Vaghri, A., & Hearn, E. H. (2012). Can lateral viscosity contrasts explain asymmetric interseismic deformation around strike-slip faults? *Bulletin of the Seismological Society of America*, *102*(2), 490–503. https://doi.org/10.1785/0120100347
Vardić, K., Clarke, P. J., & Whitehouse, P. L. (2022). A GNSS velocity field for crustal deformation studies: The influence of glacial isostatic adjustment on plate motion models. *Geophysical Journal International*, *231*(1), 426–458. https://doi.org/10.1093/gji/ggac047
Vergnolle, M., Calais, E., & Dong, L. (2007). Dynamics of continental deformation in Asia. *Journal of Geophysical Research*, *112*(B11), B11403. https://doi.org/10.1029/2006JB004807
Vernant, P. (2015). What can we learn from 20 years of interseismic GPS measurements across strike-slip faults? *Tectonophysics*, *644–645*, 22–39. https://doi.org/10.1016/j.tecto.2015.01.013
Vigny, C., Simons, W. J. F., Abu, S., Bamphenyu, R., Satirapod, C., Choosakul, N., et al. (2005). Insight into the 2004 Sumatra–Andaman earthquake from GPS measurements in southeast Asia. *Nature*, *436*(7048), 201–206. https://doi.org/10.1038/nature03937
Wahr, J., Khan, S. A., van Dam, T., Liu, L., van Angelen, J. H., van den Broeke, M. R., & Meertens, C. M. (2013). The use of GPS horizontals for loading studies, with applications to northern California and southeast Greenland. *Journal of Geophysical Research: Solid Earth*, *118*(4), 1795–1806. https://doi.org/10.1002/jgrb.50104
Wallace, L., Beavan, M. J., McCaffrey, R., & Darby, D. (2004). Subduction zone coupling and tectonic block rotations in the North Island, New Zealand. *Journal of Geophysical Research*, *109*(B12), B12406. https://doi.org/10.1029/2004JB003241
Wang, J., Penna, N. T., Clarke, P. J., & Bos, M. S. (2020). Asthenospheric anelasticity effects on ocean tide loading around the East China Sea observed with GPS. *Solid Earth*, *11*(1), 185–197. https://doi.org/10.5194/se-11-185-2020
Wang, K., Hu, Y., & He, J. (2012). Deformation cycles of subduction earthquakes in a viscoelastic Earth. *Nature*, *484*(7394), 327–332. https://doi.org/10.1038/nature11032
Wang, M., & Shen, Z.-K. (2020). Present-day crustal deformation of continental China derived from GPS and its tectonic implications. *Journal of Geophysical Research: Solid Earth*, *125*(2), e2019JB018774. https://doi.org/10.1029/2019JB018774
Wang, R., Lorenzo-Martín, F., & Roth, F. (2006). PSGRN/PSCMP—A new code for calculating co- and post-seismic deformation, geoid and gravity changes based on the viscoelastic-gravitational dislocation theory. *Computers & Geosciences*, *32*(4), 527–541. https://doi.org/10.1016/j.cageo.2005.08.006
Wang, W., Qiao, X., Wang, D., Chen, Z., Yu, P., Lin, M., & Chen, W. (2019). Spatiotemporal noise in GPS position time-series from crustal movement observation network of China. *Geophysical Journal International*, *216*(3), 1560–1577. https://doi.org/10.1093/gji/ggy506
Wang, W., Sun, W., Wu, Y., & Gu, G. (2014). Modification of fault slip models of the Mw 9.0 Tohoku Earthquake by far field GPS observations. *Journal of Geodynamics*, *75*, 22–33. https://doi.org/10.1016/j.jog.2014.01.005
Watson, A. R., Elliott, J. R., Lazecký, M., Maghsoudi, Y., McGrath, J. D., & Walters, R. J. (2024). An InSAR-GNSS velocity field for Iran. *Geophysical Research Letters*, *51*(10), e2024GL108440. https://doi.org/10.1029/2024GL108440
Wdowinski, S., Bock, Y., Zhang, J., Fang, P., & Genrich, J. (1997). Southern California permanent GPS geodetic array: Spatial filtering of daily positions for estimating coseismic and postseismic displacements induced by the 1992 Landers earthquake. *Journal of Geophysical Research*, *102*(B8), 18057–18070. https://doi.org/10.1029/97JB01378
Wdowinski, S., Smith-Konter, B., Bock, Y., & Sandwell, D. (2007). Diffuse interseismic deformation across the Pacific-North America plate boundary. *Geology*, *35*(4), 311–314. https://doi.org/10.1130/G22938A.1
Wedmore, L. N., Biggs, J., Floyd, M., Fagereng, Å., Mdala, H., Chindandali, P., et al. (2021). Geodetic constraints on cratonic microplates and broad strain during rifting of thick southern African lithosphere. *Geophysical Research Letters*, *48*(17), e2021GL093785. https://doi.org/10.1029/2021GL093785
Weiss, J. P., Steigenberger, P., & Springer, T. (2017). Orbit and clock product generation. In *Springer handbook of global navigation satellite systems* (pp. 983–1010). https://doi.org/10.1007/978-3-319-42928-1_34
Williams, C. R., Arnadottir, T., & Segall, P. (1993). Coseismic deformation and dislocation models of the 1989 loma Prieta earthquake derived from global positioning system measurements. *Journal of Geophysical Research*, *98*(B3), 4567–4578. https://doi.org/10.1029/92JB02294
Williams, S. D. P. (2003). Offsets in global positioning system time series. *Journal of Geophysical Research*, *108*(B6), 2310. https://doi.org/10.1029/2002JB002156
Williams, S. D. P. (2008). Cats: GPS coordinate time series analysis software. *GPS Solutions*, *12*(2), 147–153. https://doi.org/10.1007/s10291-007-0086-4
Williams, S. D. P., Bock, Y., Fang, P., Jamason, P., Nikolaidis, R. M., Prawirodirdjo, L., et al. (2004). Error analysis of continuous GPS position time series. *Journal of Geophysical Research*, *109*(B3), B03412. https://doi.org/10.1029/2003JB002741
Wu, D., Yan, H., & Yuan, S. (2018). L1 regularization for detecting offsets and trend change points in GNSS time series. *GPS Solutions*, *22*(3), 88. https://doi.org/10.1007/s10291-018-0756-4

15252027, 2024, 7, Downloaded from https://agupubs.onlinelibrary.wiley.com/doi/10.1029/2024GC011567, Wiley Online Library on [16/07/2024]. See the Terms and Conditions (https://onlinelibrary.wiley.com/terms-and-conditions) on Wiley Online Library for rules of use; OA articles are governed by the applicable Creative Commons License

Wu, Q., Pan, Y., Ding, H., Xiao, Y., & He, X. (2023). Quantifying the effect of non-seasonal non-tidal loadings on background noise properties of GPS vertical displacements in mainland China. *Measurement*, *217*, 113007. https://doi.org/10.1016/j.measurement.2023.113007

Wu, W., Zhang, Y., Hao, X., & Liu, J. (2024). Three-dimensional displacement and slip distribution of the 2021 Mw 7.4 Maduo (Tibetan Plateau) earthquake determined by GNSS and InSAR. *Journal of Asian Earth Sciences*, *270*, 106188. https://doi.org/10.1016/j.jseaes.2024.106188

Wu, Y., Jiang, Z., Yang, G., Wei, W., & Liu, X. (2011). Comparison of GPS strain rate computing methods and their reliability. *Geophysical Journal International*, *185*(2), 703–717. https://doi.org/10.1111/j.1365-246X.2011.04976.x

Xiang, Y., Wang, H., Chen, Y., & Xing, Y. (2021). GNSS imaging of strain rate changes and vertical crustal motions over the Tibetan plateau. *Remote Sensing*, *13*(23), 4937. https://doi.org/10.3390/rs13234937

Xiong, Z., Zhuang, J., Zhou, S., Matsu'ura, M., Hao, M., & Wang, Q. (2021). Crustal strain-rate fields estimated from GNSS data with a Bayesian approach and its correlation to seismic activity in Mainland China. *Tectonophysics*, *815*, 229003. https://doi.org/10.1016/j.tecto.2021.229003

Xu, K., Liu, J., Liu, X., Liu, J., & Zhao, F. (2020). Multiscale crustal deformation around the southeastern margin of the Tibetan Plateau from GNSS observations. *Geophysical Journal International*, *223*(2), 1188–1209. https://doi.org/10.1093/gji/ggaa289

Xu, X., Dong, D., Fang, M., Zhou, Y., Wei, N., & Zhou, F. (2017). Contributions of thermoelastic deformation to seasonal variations in GPS station position. *GPS Solutions*, *21*(3), 1265–1274. https://doi.org/10.1007/s10291-017-0609-6

Yan, H., Chen, W., Zhu, Y., Zhang, W., & Zhong, M. (2009). Contributions of thermal expansion of monuments and nearby bedrock to observed GPS height changes. *Geophysical Research Letters*, *36*(13), L13301. https://doi.org/10.1029/2009GL038152

Yan, J., Dong, D., Bürgmann, R., Materna, K., Tan, W., Peng, Y., & Chen, J. (2019). Separation of sources of seasonal uplift in China using independent component analysis of GNSS time series. *Journal of Geophysical Research: Solid Earth*, *124*(11), 11951–11971. https://doi.org/10.1029/2019JB018139

Yong-Ge, W. A. N., Shen, Z. K., Wang, M., Zhang, Z. S., Gan, W. J., Wang, Q. L., & Sheng, S. Z. (2008). Coseismic slip distribution of the 2001 Kunlun mountain pass west earthquake constrained by GPS and InSAR data. *Chinese Journal of Geophysics*, *51*(4), 753–764. https://doi.org/10.1002/cjg2.1268

You, X., & Yuan, L. (2021). The sensitivity of ocean tide loading displacements to the structure of the upper mantle and crust of Taiwan Island. *Earth Planets and Space*, *73*(1), 193. https://doi.org/10.1186/s40623-021-01525-x

Zhao, B., Wang, W., Yang, S., Peng, M., Qiao, X., Du, R., & Nie, Z. (2012). Far field deformation analysis after the Mw9.0 Tohoku earthquake constrained by cGPS data. *Journal of Seismology*, *16*(2), 305–313. https://doi.org/10.1007/s10950-011-9271-6

Zhao, G., Meng, G., Wu, W., Su, X., & Pan, Z. (2022). Earthquake potential assessment around the southeastern Tibetan plateau based on seismic and geodetic data. *Pure and Applied Geophysics*, *179*(1), 11–44. https://doi.org/10.1007/s00024-021-02917-6

Zhao, Q., Chen, Q., van Dam, T., She, Y., & Wu, W. (2023). The vertical velocity field of the Tibetan Plateau and its surrounding areas derived from GPS and surface mass loading models. *Earth and Planetary Science Letters*, *609*, 118107. https://doi.org/10.1016/j.epsl.2023.118107

Zhong, S. (2001). Role of ocean-continent contrast and continental keels on plate motion, net rotation of lithosphere, and the geoid. *Journal of Geophysical Research*, *106*(B1), 703–712. https://doi.org/10.1029/2000jb900364

Zumberge, J. F., Heflin, M. B., Jefferson, D. C., Watkins, M. M., & Webb, F. H. (1997). Precise point positioning for the efficient and robust analysis of GPS data from large networks. *Journal of Geophysical Research*, *102*(B3), 5005–5017. https://doi.org/10.1029/96JB03860

15252027, 2024, 7, Downloaded from https://agupubs.onlinelibrary.wiley.com/doi/10.1029/2024GC011567, Wiley Online Library on [16/07/2024]. See the Terms and Conditions (https://onlinelibrary.wiley.com/terms-and-conditions) on Wiley Online Library for rules of use; OA articles are governed by the applicable Creative Commons License